J. Fluid Mech. (2023), *vol.* 972, A14, doi:10.1017/jfm.2023.691

Multiscale dynamics in streamwise-rotating channel turbulence

Running Hu[1,2], **Xinliang Li**[1,2] **and Changping Yu**[1,†]

[1]LHD, Institute of Mechanics, Chinese Academy of Sciences, Beijing 100190, PR China

[2]School of Engineering Science, University of Chinese Academy of Sciences, Beijing 100049, PR China

(Received 9 September 2022; revised 25 June 2023; accepted 11 August 2023)

In this paper the multiscale dynamics of streamwise-rotating channel turbulence is studied through direct numerical simulations. Using the generalized Kolmogorov equation, we find that as rotation becomes stronger, the turbulence in the buffer layer is obviously reduced by the intense spatial turbulent convection. On the contrary, in other layers, the turbulence is strengthened mainly by the modified production peak, the intense spatial turbulent convection and the suppressed forward energy cascades. It is also discovered that under a system rotation, small- and large-scale inclined structures have different angles with the streamwise direction, and the difference is strengthened with increasing rotation rates. The multiscale inclined structures are further confirmed quantitatively through a newly defined angle based on the velocity vector. Through the budget balance of Reynolds stresses and the hairpin vortex model, it is discovered that the Coriolis force and the pressure–velocity correlation are responsible for sustaining the inclined structures. The Coriolis force directly decreases the inclination angles but indirectly induces inclined structures in a more predominant way. The pressure–velocity correlation term is related to the strain rate tensor. Finally, the anisotropic generalized Kolmogorov equation is used to validate the above findings and reveals that the multiscale behaviours of the inclined structures are mainly induced by the mean spanwise velocity gradients.

Key words: rotating turbulence, turbulence simulation

1. Introduction

Wall-bounded turbulent flows subject to rotation are important in terms of engineering (Jiménez 2011; Jing & Ducoin 2020). When rotation is coupled to the wall-bound

† Email address for correspondence: cpyu@imech.ac.cn

turbulence as a body force, the near-wall dynamics is different from those in traditional boundary layers (Jiménez & Pinelli 1999).

The study of rotation in wall-bound turbulence began with experiments of the spanwise-rotating channel (Johnston, Halleent & Lezius 1972). In channel turbulence with spanwise rotation, the symmetry in the wall-normal direction is broken (Kristoffersen & Andersson 1993). Oberlack (2001) used group analyses to deduce the linear profiles of the mean velocity. The linear profiles and related scaling laws were further discussed by Xia, Shi & Chen (2016). Additionally, couples of Taylor–Görtler-like (TGL) vortices were found in spanwise-rotating channel turbulence (Dai, Huang & Xu 2016). Brethouwer (2017) found that the intensity and size of the TGL vortices decrease at high rotation rates. In streamwise-rotating channel turbulence the symmetry is still conserved (Oberlack, Cabot & Rogers 1999). However, a secondary mean flow, i.e. a mean flow perpendicular to the streamwise direction, is induced by streamwise rotation (Wu & Kasagi 2004; Dai, Huang & Xu 2019). The secondary flow is inverted around the channel centre (Yang, Su & Wu 2010). Such an inverse secondary mean flow has not been observed in experiments due to the measurement accuracy (Recktenwald *et al.* 2007; Alkishriwi, Meinke & Schröder 2008; Recktenwald, Alkishriwi & Schröder 2009). However, Oberlack *et al.* (2006) used group analyses to analytically study streamwise-rotating channel turbulence and qualitatively found the existence of the inverse secondary mean flow. Masuda, Fukuda & Nagata (2008) further verified this through instability analysis. Yang *et al.* (2010) used helical wave decomposition to deduce the inviscid inertial wave solution, which gave a trigonometric profile. This prediction is suitable for the spanwise mean velocity in the bulk region but is not reasonable for the streamwise mean velocity due to the possible effects of the external mean pressure gradient. Yang *et al.* (2020*a*) studied the non-monotonic tendency of the spanwise mean velocity with increasing rotation rates and attributed it to the self-constraint mechanism of the Reynolds stress $\langle u_2 u_3 \rangle$. Yang *et al.* (2018) discussed the pressure fluctuations in this flow. Additionally, since streamwise-rotating channel turbulence is a typical chirality-asymmetric flow, helicity ($H = \boldsymbol{u} \cdot \boldsymbol{\omega}$) is also an important quantity here. Recently, Yu *et al.* (2022) and Yan, Li & Yu (2022) discussed the distribution and budget balance of the helicity in streamwise-rotating channel turbulence. In terms of coherent structures, Yang *et al.* (2010) found that when the rotation number $Ro_\tau = 30$, the inclined vortex columns moving downstream are likely the carriers of inertial waves. Yang & Wang (2018) found that TGL vortices exist when $Ro_\tau = 150$. These TGL vortices have negligible inclination angles and are almost aligned with the rotation axis x_1. Their spanwise length scale is independent of Ro_τ, but their streamwise length scale exhibits a considerable dependence on Ro_τ (Yang & Wang 2018). Dai *et al.* (2019) studied the coherent structures in the streamwise-rotating channel through direct numerical simulations (DNS) and large eddy simulations. They found that the elongated streamwise vortices are tilted toward the spanwise direction, and the inclination angle initially increases and then decreases with increasing rotation rates. However, the mechanisms for this non-monotonic tendency are still not clear.

Turbulence is in fact a multiscale physical problem. To study the interscale dynamics, various approaches have been applied by researchers (Lumley 1964; Danaila *et al.* 2001; Dunn & Morrison 2003). Utilizing the Fourier transform, Lumley (1964) first derived the spectral energy equation for the interscale energy transfer. Bolotnov *et al.* (2010) statistically studied the interscale energy transfer in channel turbulence with a low Reynolds number. Dunn & Morrison (2003) used orthogonal wavelets to analyse spatial and interscale (both forward and backward) energy transfers. However, these approaches do not allow for a distinction between spatial and interscale transfers in the wall-normal direction, which can be addressed using the second-order structure function and its budget balance (Cimarelli *et al.* 2016; Mizuno 2016). The second-order structure function has been used by Kolmogorov (1941) to study the energy cascades in homogeneous isotropic turbulence, and its evolution equation is known as the Kolmogorov equation. The second-order structure function can be interpreted as the amount of energy of a given scale at a certain position and is also called the scale energy (Marati, Casciola & Piva 2004; Cimarelli *et al.* 2015, 2016). The approach was first generalized to channel turbulence by Danaila *et al.* (2001) and further extended to general flows by Hill (2002). In these flows, the extended budget equation is called the generalized Kolmogorov equation (GKE). Then, the GKE was used to study the energy cascades in channel turbulence by Marati *et al.* (2004). Based on the GKE, Cimarelli, De Angelis & Casciola (2013) found the near-wall turbulence regeneration cycle and the outer self-sustaining mechanism in channel turbulence. Cimarelli *et al.* (2015) found that the energy source in the outer layer modifies nearby energy fluxes and then affects the energy transfers in the vicinity of the wall. Cimarelli *et al.* (2016) further used the GKE to study the interscale energy transfer in the wall-normal direction and found two ways of interscale energy transfer, consistent with the classical attached vortex model (Marusic & Monty 2019). The GKE has also been used to study the dynamics in flows with separation and reattachment (Mollicone *et al.* 2018). The anisotropic generalized Kolmogorov equation (AGKE), i.e. the budget equation for the second-order structure function of Reynolds stresses, was first investigated by Gatti *et al.* (2020), who took more details of the interscale dynamics into consideration. Notably, even if the scale energy is strictly related to the energy spectra, it is not an intensive quantity (Cimarelli *et al.* 2015). At small scales, the scale energy could be approximately treated as the eddy intensity of these scales. However, this interpretation is not suitable when the separation is sufficiently large. In fact, as the scale tends to be infinite, the scale energy is reduced to four times the turbulence kinetic energy (TKE) (Marati *et al.* 2004). Yang *et al.* (2010) used helical wave decomposition to investigate the interscale dynamics in streamwise-rotating channel turbulence. However, this approach cannot give the spatial-local interscale dynamics, such as the near-wall dynamics. Yang *et al.* (2020*b*) took the interscale transfer into consideration via the budget balance for the spectral TKE. They discussed the sustaining mechanisms of the TGL vortices and found that four key processes are responsible for sustaining the motion of large-scale TGL vortices.

In summary, in streamwise-rotating channel turbulence, the study of near-wall multiscale dynamics under moderate rotation rates is still insufficient. This paper focuses on the coupling effects of moderate rotation and boundary layers on turbulence. Specifically, basic turbulence statistics are first examined, where we find the scale discrepancy of inclined structures. To be more concrete, the scale discrepancy is further identified using the newly defined angle based on the velocity vector. The focus then shifts to the sustaining mechanisms of the inclined structures. Several key terms in the Reynolds stress budget balance are identified, and corresponding physical processes are illustrated through ejections and sweeps in the hairpin vortex model. Finally, a mechanism responsible for the scale discrepancies is given utilizing the AGKE.

The paper is organized as follows. We give the details of the simulations and basic statistics in § 2. Next, in § 3 we analyse the basic interscale dynamics through the scale energy and GKE. Section 4 gives the main results of this paper, where we identify the multiscale inclined structures and their sustaining mechanisms. Finally, conclusions are given in § 5.

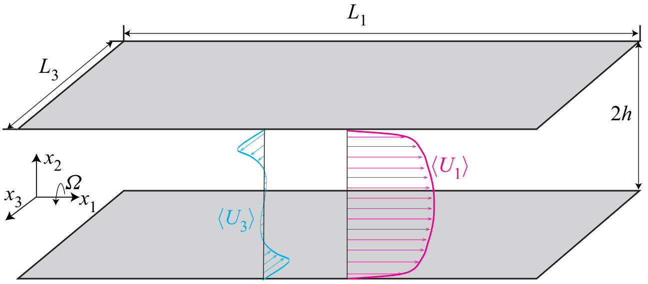

Figure 1. Sketch of the streamwise-rotating channel turbulence. The red and blue lines are the mean velocity profiles.

2. Numerical simulations

2.1. *Numerical set-up*

The incompressible Navier–Stokes equations are

$$\left.\begin{aligned}\frac{\partial U_i}{\partial t}+U_j\frac{\partial U_i}{\partial x_j}&=-\frac{1}{\rho}\frac{\partial p}{\partial x_i}+\nu\frac{\partial^2 U_i}{\partial x_j\partial x_j}+2\epsilon_{ij1}U_j\Omega-\frac{\Pi_0}{\rho}\delta_{i1},\\ \frac{\partial U_i}{\partial x_i}&=0,\end{aligned}\right\}\tag{2.1}$$

where U_i is the velocity, p is the total pressure including the centrifugal effects (Davidson 2013), ρ is the density, ν is the kinematic viscosity, Ω is the rotation rate in the streamwise direction, Π_0 is a constant streamwise pressure gradient that drives the flow, δ_{ij} is the Kronecker delta and ϵ_{ijk} is the Levi-Civita symbol. Equation (2.1) is solved through a pseudo-spectral code using Fourier series in the streamwise and spanwise directions and Chebyshev polynomials in the wall-normal direction. The 3/2 rule is utilized to remove aliasing errors. A third-order time-splitting method is used for time advancement. More details can be found in previous works (Deng & Xu 2012; Yang & Wang 2018). A sketch of the computational configuration and the mean velocities is given in figure 1.

There are two non-dimensional parameters based on the friction velocity, i.e. the Reynolds and rotation numbers

$$Re_\tau=u_\tau h/\nu,\quad Ro_\tau=2\Omega h/u_\tau,\tag{2.2a,b}$$

where u_τ is the friction velocity and $h=1$ is the channel half-width. In addition, the friction velocity u_τ and the viscous length scale ν/u_τ are used to normalize the quantities in the following analyses, which are marked by the superscript '+'. Our DNS data include five cases, in which Ro_τ ranges from 0 to 60 and $Re_\tau=180$ or 395. Except for ST30S and ST60S, the computational domains of the cases are selected based on the third criterion of Yang & Wang (2018), which has been verified by Yu *et al.* (2022). Cases ST30S and ST60S have relatively small streamwise sizes. The data used in this paper are time averaged over 40 h/u_τ after reaching the statistical steady state. As verified through the approach of Russo & Luchini (2017), the time slices are independent of each other. The relative standard deviation of the data is less than 1 %. In addition, the reliability of the data can also be confirmed through the balance of the budget equation in the following analysis. The parameters are summarized in table 1.

Case	$L_1 \times 2h \times L_3$	$N_1 \times N_y \times N_3$	Re_τ	Ro_τ
ST00	$32\pi \times 2 \times 8\pi$	$1024 \times 128 \times 512$	180	0
ST07	$32\pi \times 2 \times 8\pi$	$1024 \times 128 \times 512$	180	7.5
ST07R	$32\pi \times 2 \times 8\pi$	$4096 \times 192 \times 1536$	395	7.5
ST15	$64\pi \times 2 \times 8\pi$	$2048 \times 128 \times 512$	180	15
ST30	$128\pi \times 2 \times 8\pi$	$4096 \times 128 \times 512$	180	30
ST30S	$64\pi \times 2 \times 8\pi$	$2048 \times 128 \times 512$	180	30
ST60S	$128\pi \times 2 \times 8\pi$	$4096 \times 128 \times 512$	180	60

Table 1. Computational descriptions of simulations.

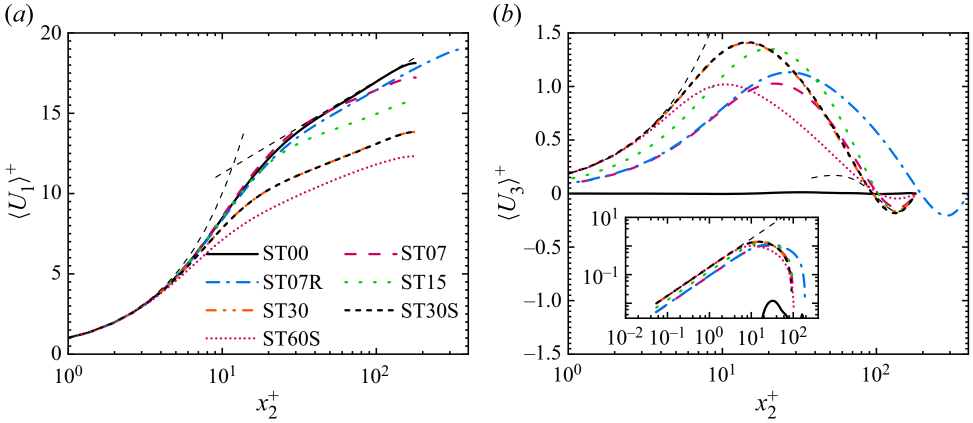

Figure 2. Profiles of mean velocities in the (*a*) streamwise and (*b*) spanwise directions. The inset in (*b*) gives the spanwise velocity in log-law coordinates. The black dashed lines in (*a*) represent the linear law and log law with Kármán constant $\kappa = 0.4$. The dashed lines in (*b*) indicate the linear law and the trigonometric function $A\sin(2\pi f(x_2^+ - 180))$ with frequency $f = 1/169.7$ and amplitude $A = 0.17$.

2.2. *Basic turbulence statistics*

Figure 2 gives the profiles of mean velocities $\langle U_1\rangle^+$ and $\langle U_3\rangle^+$, where $\langle\cdot\rangle$ represents averaging over time and the $x_1 - x_3$ plane. In the following analysis, if the non-dimensional wall-normal coordinates (x_2^+) are used, then the data in the upper domain ($x_2 \in [0, 1]$) are discussed by default. The black dashed lines in figure 2(*a*) represent the linear law and log law with the Kármán constant $\kappa = 0.4$. The black dashed lines in figure 2(*b*) indicate the linear law with an amplitude of 0.18 as well as the trigonometric function $A\sin(2\pi f(x_2^+ - 180))$ with $f = 1/169.7$ and $A = 0.17$. As shown in figure 2, ST30 and ST30S have the same mean velocity profile. It will also be shown in § 3.1 that the second-order structure functions of the two cases are also nearly identical. Since the streamwise size of ST60S increases by the same ratio of Ro_τ compared with ST30S, ST60S can at least provide reliable basic statistics. As shown in figure 2(*a*), rotation does not affect the linear law of $\langle U_1\rangle^+$ in the viscous sublayer. In the log-law layer the profile of $\langle U_1\rangle^+$ is still logarithmic, while the amplitudes are suppressed by rotation. In figure 2(*b*) the spanwise mean velocity $\langle U_3\rangle^+$ is induced by rotation. In the bulk region, $\langle U_3\rangle^+$ is reversed and has a trigonometric profile, which is the inviscid inertial wave solution of streamwise-rotating channel turbulence (Yang *et al.* 2010). Furthermore, $\langle U_3\rangle^+$ in the viscous sublayer has a linear profile, which is also confirmed in the inset of figure 2(*b*).

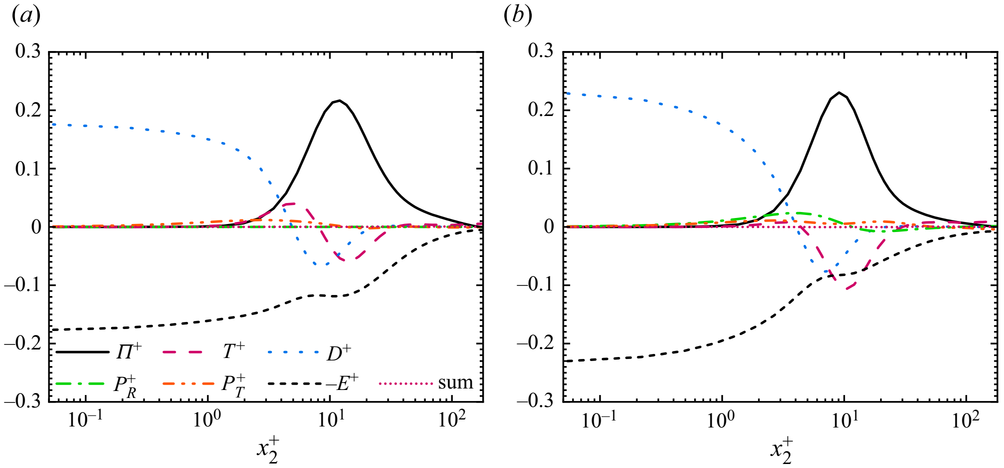

Figure 3. Budget balance of the TKE: (*a*) ST00, (*b*) ST30.

Up to rotation number $Ro_\tau = 30$, the stronger the rotation is, the faster $\langle U_3\rangle^+$ increases. However, the tendency is reversed as Ro_τ becomes higher. Similar results have also been found by Yang *et al.* (2020*a*).

The budget equation of the TKE can be written as

$$\underbrace{-\langle u_1u_2\rangle\frac{\mathrm{d}\langle U_1\rangle}{\mathrm{d}x_2}-\langle u_2u_3\rangle\frac{\mathrm{d}\langle U_3\rangle}{\mathrm{d}x_2}}_{\Pi}\underbrace{-\frac{1}{2}\frac{\mathrm{d}}{\mathrm{d}x_2}\langle u_iu_iu_2\rangle}_{T}+\underbrace{\frac{\nu}{2}\frac{\mathrm{d}^2}{\mathrm{d}x_2^2}\langle u_iu_i\rangle}_{D}$$

$$\underbrace{-\nu\left\langle\frac{\partial u_i}{\partial x_j}\frac{\partial u_i}{\partial x_j}\right\rangle}_{-E}\underbrace{-\frac{1}{\rho}\frac{\mathrm{d}}{\mathrm{d}x_2}\langle p_Ru_2\rangle}_{P_R}\underbrace{-\frac{1}{\rho}\frac{\mathrm{d}}{\mathrm{d}x_2}\langle p_Tu_2\rangle}_{P_T}=0, \tag{2.3}$$

where Π is the production and represents the interaction between the mean and fluctuating fields, T is the turbulent convection, D is the viscous diffusion, E is the pseudo-dissipation, and P_R and P_T are the pressure–velocity correlation terms related to the rotation effects and turbulent convection, respectively. The pressure components p_R and p_T are obtained through pressure decomposition (Yang *et al.* 2018; Hu, Li & Yu 2022). In the TKE budget equation, rotation modifies the production by inducing non-zero spanwise mean velocity $\langle U_3\rangle$.

The TKE budget balance is given in figure 3. The viscous diffusion D and pseudo-dissipation E near the wall ($x_2^+ \lessapprox 1$) are intensified by rotation. According to the definition of D $(=\nu\mathrm{d}^2\langle u_iu_i\rangle/\mathrm{d}x_2^2/2)$ and the distribution of the Reynolds stresses given by Yang & Wang (2018), the intensified viscous effects near the wall can be attributed to the strong spanwise TKE $\langle u_3u_3\rangle$ induced by rotation. Additionally, as rotation becomes stronger, the E above the buffer layer ($x_2^+ \gtrapprox 10$) decreases, while the production Π is less affected. This could be related to the reduced dissipation induced by rotation in homogeneous turbulence (Mininni, Alexakis & Pouquet 2009). In contrast to the pseudo-dissipation E, the turbulent convection T and viscous diffusion D are strengthened by rotation. For the turbulent convection T, with rotation becoming stronger, the flux toward the wall decreases, while that toward the channel centre increases. The more intensive flux toward the channel centre is consistent with the stronger TKE at this location observed by Yang & Wang (2018). For viscous diffusion D, larger fluxes lead to stronger TKE near the wall, especially $\langle u_3u_3\rangle$. In turn, the viscous effects are strengthened by $\langle u_3u_3\rangle$, which has been discussed above. The pressure terms P_R and P_T are negligible here, but they mainly redistribute energy among different TKE components (Yang *et al.* 2020*b*).

3. Multiscale analysis of the streamwise-rotating channel

The above results are about single-point statistics. However, turbulence is a multiscale process. In this section we introduce the effects of scales through the scale energy and its budget balance.

3.1. *Scale energy*

The velocity increment with centre $\boldsymbol{X}$ and separation $\boldsymbol{r}$ is written as

$$\delta u_i(\boldsymbol{X}, \boldsymbol{r}) = u_i(\boldsymbol{x}) - u_i(\boldsymbol{x}'), \tag{3.1}$$

where $\boldsymbol{x} = \boldsymbol{X} + \frac{1}{2}\boldsymbol{r}$ and $\boldsymbol{x}' = \boldsymbol{X} - \frac{1}{2}\boldsymbol{r}$. For convenience, let u_i and p denote the flow field variables at $\boldsymbol{x}$ and u_i' and p' denote the corresponding variables at $\boldsymbol{x}'$ hereafter. The scale energy is then written as

$$\langle \delta u^2\rangle = \langle \delta u^2\rangle(X_2, \boldsymbol{r}) = \langle \delta u_i(\boldsymbol{X}, \boldsymbol{r})\delta u_i(\boldsymbol{X}, \boldsymbol{r})\rangle. \tag{3.2}$$

This paper mainly focuses on the interscale transfers in the streamwise direction, and only the separations $\boldsymbol{r}$ with $r_2 = 0$ are considered here. Since $\langle \delta u^2\rangle = 2\langle u_iu_i\rangle - 2\langle u_iu_i'\rangle$, at a given scale $r = (r_1^2 + r_3^2)^{1/2}$, the direction with the minimum scale energy $\min\{\langle \delta u^2\rangle\}$ has the maximum two-point correlation $\max\{\langle u_iu_i'\rangle\}$, indicating the average inclination angle of vortices at this scale r.

The scale energy is shown in figure 4, where panel (*a*) gives the results with respect to r_1^+ in the viscous sublayer, and panels (*b*) and (*c*) give the results with respect to r_1^+ and r_3^+ in the log-law layer, respectively. Cases ST30S and ST30 have almost the same results. As shown in figure 4(*a*), in the viscous sublayer, with stronger rotation rates, the scale energy becomes larger. In addition, as rotation intensifies, the scale energy has a narrower streamwise scale range, which indicates that rotation shortens the streamwise structures in the viscous sublayer. In the log-law layer the production and the pseudo-dissipation approximately balance each other (Marati *et al.* 2004). For scales smaller than the detached scale ($r^+ \lessapprox x_2^+$), the effects of the wall diminish, and the turbulence here is approximately locally isotropic in non-rotating channel turbulence (Casciola *et al.* 2005; Cimarelli *et al.* 2015). Similarly, the transfers in the log-law layer of streamwise-rotating channel turbulence are expected to be related to those in homogeneous rotating turbulence. As shown in figure 4(*b*), in the log-law layer, rotation increases the slope of the scale energy with respect to r_1^+ and strongly elongates the streamwise vortices. Roughly speaking, in the log-law layer, as rotation becomes stronger, the slopes near $r_1^+ \sim 50$ change from $r_1^{+2/3}$ to r_1^+. The two slopes are consistent with the energy spectra $k^{-5/3}$ and k^{-2}. The latter scaling law (r_1^+ and k^{-2}) has been confirmed by previous studies on homogeneous rotating turbulence (Yeung & Zhou 1998; Smith & Waleffe 1999; Mininni *et al.* 2009). As shown in figure 4(*c*), rotation has a negligible effect on the behaviour of the scale energy for spanwise separations, consistent with the results of Yang & Wang (2018).

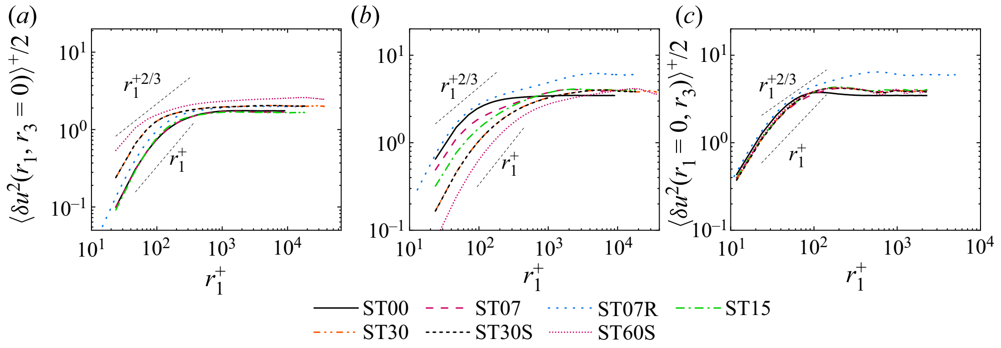

Figure 4. Scale energy profiles: (*a*) $\langle \delta u^2(r_1, r_3 = 0)\rangle^+/2$ in the viscous sublayer ($x_2^+ = 3.4$ for ST07R and $x_2^+ = 3.5$ for other cases), (*b*) $\langle \delta u^2(r_1, r_3 = 0)\rangle^+/2$ in the log-law layer ($x_2^+ = 81.6$ for ST07R and $x_2^+ = 80.0$ for other cases), (*c*) $\langle \delta u^2(r_1 = 0, r_3)\rangle^+/2$ in the log-law layer.

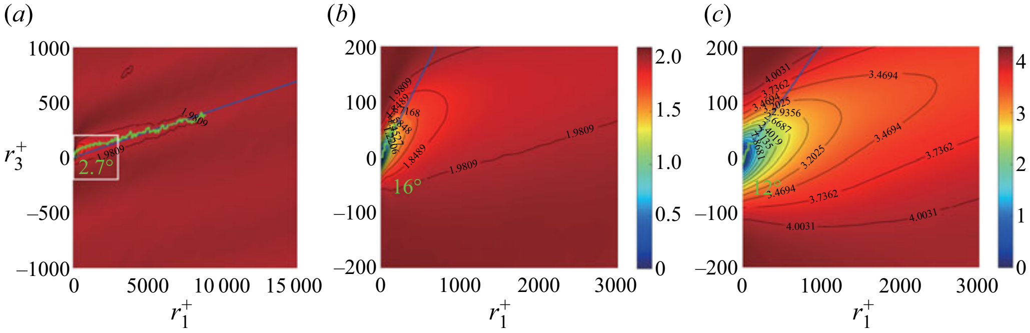

Figure 5. Scale energy $\langle \delta u^2\rangle^+/2$ of ST30 on the $r_1^+ - r_3^+$ plane. (*a*) Large-scale distribution in the viscous sublayer ($x_2^+ = 3.5$). (*b*) Small-scale distribution in the viscous sublayer. (*c*) Small-scale distribution in the log-law layer ($x_2^+ = 80.0$). The green lines represent the directions of the coherent structures at certain scales. The green labels and blue lines are the fitting results of the green lines.

This could be attributed to the fact that the wall constrains the development of wall-normal and spanwise scales. Without rotation, the maximum of the scale energy corresponds to the spanwise scale $r_3^+ = 117.8$. When rotation is introduced, this spanwise scale is modified to $r_3^+ \approx 200$ and is insensitive to the rotation rates. The comparison of ST07R and ST07 gives the effects of the Reynolds numbers. In the viscous sublayer and the log-law layer, the distribution is not obviously modified. However, the amplitudes of ST07R are slightly larger, especially for the results in the log-law layer.

Figure 5 shows the scale energy in the $r_1 - r_3$ plane in the viscous sublayer and log-law layer. The green lines are obtained from a series of (r_1, r_3) with $\min\{\langle \delta u^2\rangle\}$ for every ring ($r_1^2 + r_3^2 = \text{const.}$). As indicated by the relation between the scale energy and the two-point correlation, at the scale $r = (r_1^2 + r_3^2)^{1/2}$, the angle $\tan^{-1}\{r_1/r_3\}$ with $\min\{\langle \delta u^2\rangle\}$ represents the direction of the vortices. Then, the green lines are fitted through the nonlinear least squares method with $R^2 > 0.8$ to obtain the inclination angles θ, which are shown by the green labels and blue lines. As shown in figures 5(*a*) and 5(*b*), in the viscous sublayer of ST30, small-scale structures ($r_1^+ \lessapprox 500$) form a strong angle with the rotation axis (up to 16°), while large-scale structures have a much smaller angle (approximately 3°). The threshold between small- and large-scale structures is determined to obtain reliable fitting results ($R^2 > 0.8$). The comparison between the results in the

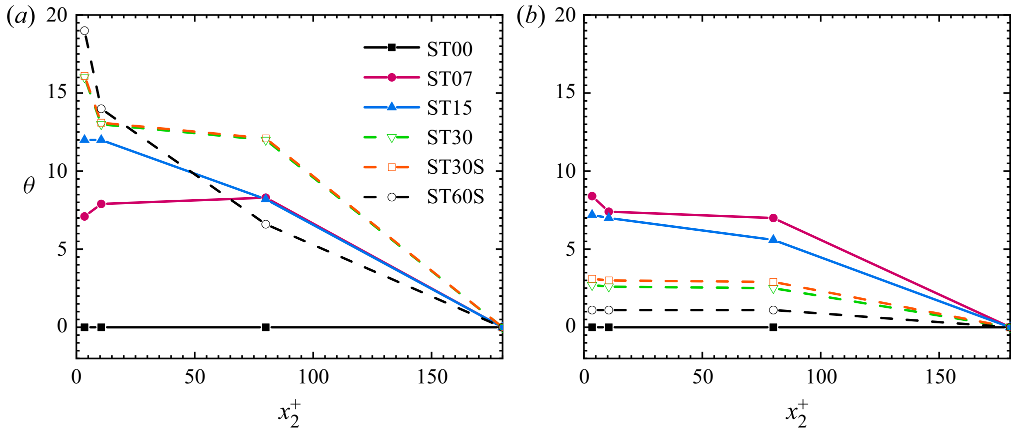

Figure 6. Inclination angles θ obtained based on the scale energy in different layers. (*a*) Small-scale inclination angles. (*b*) Large-scale inclination angles.

viscous sublayer (figure 5*b*) and those in the log-law layer (figure 5*c*) shows that energetic motions are distributed over a wider scale range in the log-law layer. In addition, as shown by the green lines, even if the small-scale inclination angles in the two layers are close to each other, the thresholds defined by strong inclination angles are far smaller in the log-law layer. The thresholds are $r_1^+ = 235.6$ and $r_3^+ = 49.0$ in the viscous sublayer, and they are $r_1^+ = 141.4$ and $r_3^+ = 23.6$ in the log-law layer. The three components of $\langle \delta u^2 \rangle$ have similar small-scale distributions, but $\langle \delta u_2^2 \rangle$ has a smaller amplitude and no obvious large-scale motion, which is not shown here for simplification.

The details about the inclination angles θ are displayed in figure 6. From the wall to the channel centre, the inclination angle θ decreases in most cases. At the channel centre, θ is exactly zero due to the antisymmetry in the wall-normal direction. Moreover, consistent with the observation of Dai *et al.* (2019), as Ro_τ becomes larger, the inclination angle of large-scale structures initially increases until $Ro_\tau = 7$ and then decreases thereafter. When $Ro_\tau = 60$, there is no apparent inclination angle ($\theta \approx 1^\circ$). Furthermore, as the rotation becomes stronger, the discrepancy between small-scale and large-scale structures is intensified. The most remarkable discrepancy occurs in the viscous sublayer of ST60S: θ at small scales is 19.0°, while at large scales is 1.1°. The multiscale inclined structures will be further quantitatively discussed in § 4.

3.2. *Basic results of the GKE*

The budget equation of the scale energy, i.e. the GKE, can be written as (Marati *et al.* 2004)

$$\underbrace{-\frac{1}{2}\frac{\partial}{\partial r_j}\langle \delta u^2 \delta u_j \rangle}_{T^{SS}} \underbrace{-\frac{1}{2}\frac{\partial}{\partial X_2}\langle \delta u^2 u_2^* \rangle}_{T^{SP}} \underbrace{-\langle \delta u_1 \delta u_2 \rangle \left\langle \frac{\partial U_1}{\partial x_2} \right\rangle^* - \langle \delta u_2 \delta u_3 \rangle \left\langle \frac{\partial U_3}{\partial x_2} \right\rangle^*}_{\varPi^S}$$

$$\underbrace{-\frac{1}{\rho}\frac{\partial}{\partial X_2}\langle \delta u_2 \delta p_R \rangle}_{P_R^S} \underbrace{-\frac{1}{\rho}\frac{\partial}{\partial X_2}\langle \delta u_2 \delta p_T \rangle}_{P_T^S} + \underbrace{\nu \frac{\partial^2}{\partial r_j \partial r_j}\langle \delta u^2 \rangle}_{D^{SS}}$$

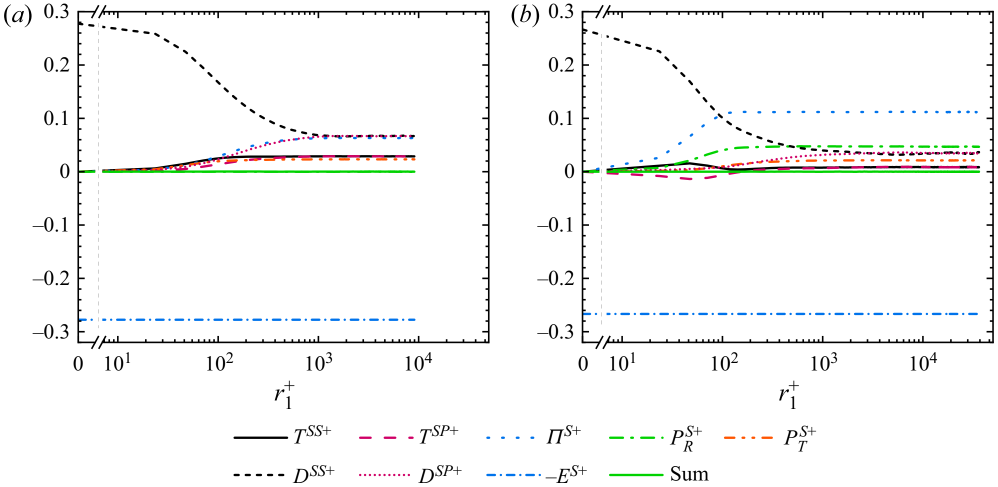

Figure 7. Budget balance of the GKE in the viscous sublayer ($x_2^+ = 3.5$). The grey dashed lines represent the breakpoint to show the origin $r_1^+ = 0$ in logarithmic coordinates. Results are shown for (*a*) ST00 and (*b*) ST30.

$$+\underbrace{\frac{\nu}{4}\frac{\partial^2}{\partial X_2^2}\langle \delta u^2 \rangle}_{D^{SP}}\ \underbrace{-\,2\langle \epsilon^* \rangle}_{-E^S} = 0, \tag{3.3}$$

where T^{SS} and T^{SP} are the turbulent convections in scale and spatial space, Π^S is the production, P_R^S and P_T^S are the pressure transfers induced by rotation and convection, D^{SS} and D^{SP} are the interscale and spatial viscous diffusions, E^S is the pseudo-dissipation, $\epsilon = \nu(\partial u_i/\partial x_j)(\partial u_i/\partial x_j)$ and '$*$' represents the average of the values at $\boldsymbol{x}$ and $\boldsymbol{x}'$.

For multiscale analyses, there are three main methods: spectral, two-point correlation and second-order structure function approaches. The spectral method is the Fourier transform of two-point correlations (Pope 2000). The relations between the second-order structure functions and the two-point correlations could be of interest and are given in Appendix A. These relations also have important practical applications in numerical postprocessing with high precision. In $\boldsymbol{r}$ space, since the field is not periodic or infinitely smooth, the partial derivatives $\partial/\partial r_1$ and $\partial/\partial r_3$ cannot be directly calculated by the Fourier transform. To overcome this difficulty, utilizing the relations between the second-order structure functions and the two-point correlations, the partial derivatives $\partial/\partial r_i$ can be expanded in terms of $\partial/\partial x_i$ and $\partial/\partial x_i'$. With the relations in Appendix A, all terms of the GKE can be written as two-point correlations. Then, the derivatives can be solved by the Fourier transform. In addition, when $r \to \infty$, the scale energy will be reduced to four times the TKE, and the GKE will be reduced to the TKE budget equation (Marati *et al.* 2004; Hu *et al.* 2022). As shown in figure 4(*c*), the scale energy in the spanwise direction is almost unaffected by rotation. Therefore, the results with $r_2 = r_3 = 0$ are the focus of this section.

The results for ST00 and ST30 in the viscous sublayer are given in figures 7(*a*) and 7(*b*), respectively. The main results are shown in logarithmic coordinates, and a breakpoint is inserted at the beginning of the abscissa to display the results at $r_1^+ = 0$.

In terms of the reliability of postprocessing, the sum of all terms is almost zero. In addition, when $r_1^+ = 0$, the viscous diffusion D^{SS} and the pseudo-dissipation E^S balance each other, while other terms are exactly zero. Specifically, as deduced by the relation (A7), when $r_1^+ = 0$, D^{SS} and E^S are two times the pseudo-dissipation E in the TKE budget equation,

$$D^{SS}(r_1 = 0, x_2) = E^S(r_1 = 0, x_2) = 2\nu \left\langle \frac{\partial u_i}{\partial x_j} \frac{\partial u_i}{\partial x_j} \right\rangle = 2E(x_2), \tag{3.4}$$

which is verified in figure 7. These observations verify our postprocessing approach that expands the GKE in terms of the two-point correlations in Appendix A.

As shown in figure 7(*a*), in the viscous sublayer of ST00, except for $-E^S < 0$ and $P_R \approx 0$, all terms are positive. The scale energy is transferred toward small scales or toward the wall by these positive terms and then dissipated by E^S. Specifically, there are four main effects in the viscous sublayer: the production Π^S, the spatial and interscale viscous transfers (D^{SP} and D^{SS}), and the pseudo-dissipation E^S. However, as shown by the TKE budget balance in figure 3, closer to the wall, Π^S is negligible compared with the viscous effects. Among the three viscous effects, D^{SP} is less important, which means that the dynamics in the viscous sublayer is spatially local (Marati *et al.* 2004). In addition, D^{SS} and D^{SP} become the same when $r_1 \to \infty$.

The results for ST30 are shown in figure 7(*b*). In ST30, Π^S is larger than that in ST00. The combination of the GKE results in figure 7 and the TKE budget balance in figure 3 suggests that Π^S is distributed closer to the wall in ST30 than in ST00. The rotation-induced pressure transfer P_R^S is positive and is an additional direct transfer toward the wall. Furthermore, except for Π^S, P_R^S and E^S, the terms are suppressed by rotation. This means that rotation strengthens the near-wall turbulence mainly by directly producing more energy (Π^S) and by the spatial pressure transfer induced by rotation (P_R^S), while other transfers between the viscous layer and the buffer layer are reduced. In fact, as shown by the TKE budget balance in figure 3, in the lower viscous layer, rotation makes the viscous effects stronger. This is mainly related to the stronger spanwise TKE $\langle u_3 u_3 \rangle$. For the scale distribution, Π^S is distributed among $r_1^+ \in (0, 10^3)$ in ST00 and among $r_1^+ \in (0, 10^2)$ in ST30. This is consistent with the scale energy in figure 4(*a*), while the discrepancy is more apparent for Π^S. In other words, rotation shortens the streamwise structures in the viscous sublayer. The results are non-trivial because rotation generally induces long streamwise coherent structures, such as TGL vortices (Yang & Wang 2018). The shorter streamwise structures are partly caused by corresponding larger inclination angles at small scales. As shown in figure 5(*a*), the inclination angle of small-scale structures in the viscous sublayer is 16°. If only the slice with $r_3^+ = 0$ is considered, then the streamwise scales become smaller.

In the buffer layer, as shown in figure 8(*a*), at large scales ($r_1^+ > 10^3$), only Π^S is positive. Therefore, energy is produced by Π^S. Then, energy is transferred to other scales by interscale transfers (D^{SS} and T^{SS}) and to other locations (up to the bulk of the flow and down to the viscous sublayer) by T^{SP} and D^{SP} or dissipated by E^S. In addition, the interscale transfers T^{SS} and D^{SS} are both positive at small scales but negative at large scales. On the one hand, energy is forward cascaded to small scales. On the other hand, if integrated in the r_1 direction, the fluxes are negative at large scales, which represents an inverse cascade. The dual cascades to smaller and larger scales are the reflection of breakdown, regeneration and coalescence of streamwise vortices (Hamilton, Kim & Waleffe 1995). Furthermore, the interscale transfers are important at small scales, while the spatial effects are mainly valid at large scales. The pressure transfers (P_R^S and P_T^S) are negligible and mainly redistribute the scale energy between different components (Yang & Wang 2018).

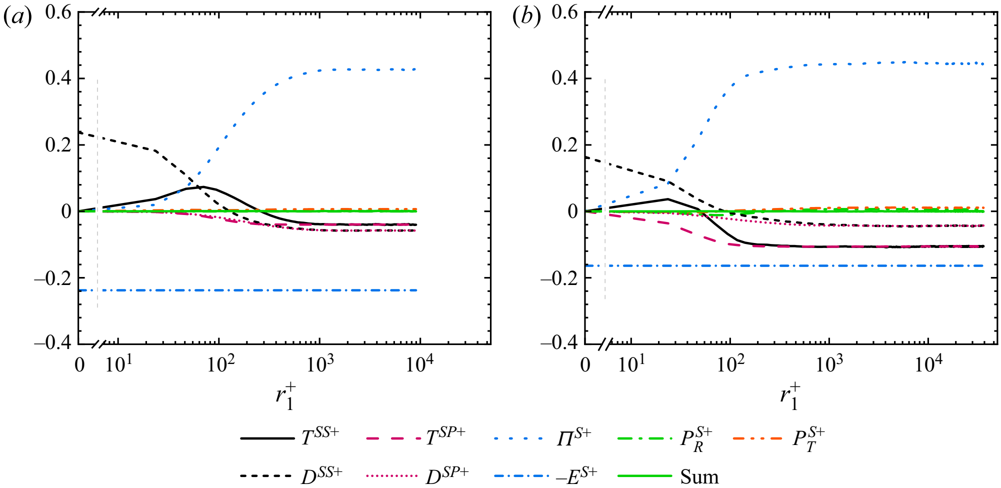

Figure 8. Budget balance of the GKE in the buffer layer ($x_2^+ = 10.5$). The grey dashed lines represent the breakpoint to show the origin $r_1^+ = 0$ in logarithmic coordinates. Results are shown for (*a*) ST00 and (*b*) ST30.

The comparison of figures 8(*a*) and 8(*b*) shows that when strong rotation is introduced, at large scales, Π^S is not affected, while E^S in the buffer layer is strongly reduced. At small scales ($r_1^+ \lesssim 10^2$), since E^S balances with the interscale transfers (T^{SS} and D^{SS}), the local interscale transfers are also reduced by rotation. At large scales ($r_1^+ \gtrsim 10^2$), the interscale and spatial turbulent convections (T^{SS} and T^{SP}) are both strengthened by rotation. These observations imply that the forward cascades to small scales in the buffer layer are reduced by rotation, and instead, the scale energy is mainly spatially transported in the wall-normal direction or inversely cascaded. Additionally, as occurs in the viscous sublayer, the scale distribution of the production is also restricted by rotation in the buffer layer, indicating the presence of strongly inclined small-scale structures here.

In the log-law layer, as shown in figure 9(*a*), when there is no rotation, Π^S is locally balanced with E^S at large scales. The spatial and interscale transfers at large scales are negligible, and the log-law layer does not obtain or lose energy. In fact, energy is produced in the buffer layer and then transferred across the log-law layer toward the channel centre (Marati *et al.* 2004). Furthermore, the comparison of figure 8(*a*) and figure 9(*a*) shows that if normalized by Π^S, the interscale transfers (D^{SS} and T^{SS}) at small scales in the log-law layer are relatively more important than those in the buffer layer. The relatively weak spatial transfers and stronger interscale transfers mean that in the log-law layer the scale energy is locally cascaded to small-scale structures.

When rotation is introduced, as shown in figure 9(*b*), the local balance of Π^S and E^S is destroyed. Remarkable spatial energy transfers (T^{SP} and P_T^S) are introduced, originating from the elongated large-scale streamwise vortices, according to the Reynolds stresses and their budget balance given by Yang & Wang (2018). Additionally, similar to the phenomena in the buffer layer, in the log-law layer the pseudo-dissipation (E^S) and the interscale transfers (D^{SS} and T^{SS}) at small scales are also reduced by rotation. In fact, as shown in figure 4(*b*), in the log-law layer the scale energy at small scales is also reduced by rotation. In terms of the scale distribution, different from the results in the former two layers, in the log-law layer the scale distribution of all terms is extended to a much wider range by rotation. This means that rotation extends the streamwise structures in the log-law layer but shortens those in the viscous sublayer and the buffer layer, which could also be associated

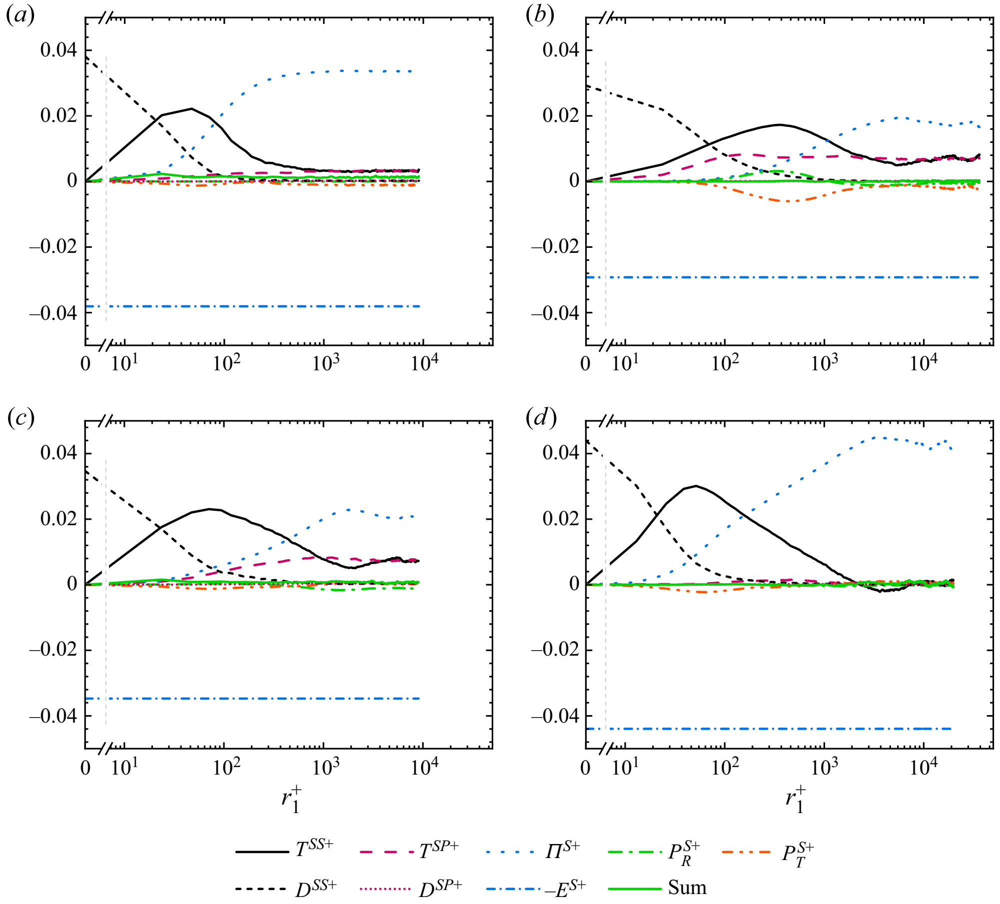

Figure 9. Budget balance of the GKE in the log-law layer ($x_2^+ = 81.6$ for ST07R and $x_2^+ = 80.0$ for other cases). The grey dashed lines represent the breakpoint to show the origin $r_1^+ = 0$ in logarithmic coordinates. Results are shown for (*a*) ST00, (*b*) ST30, (*c*) ST07, (*d*) ST07R.

with the smaller inclination angle and narrower small-scale range in the log-law layer, as shown by the scale energy in figure 5(*b*,*c*).

Cases ST07 and ST07R are compared here to examine the effects of the Reynolds numbers. Figure 9(*c*,*d*) shows that the difference in the GKE results is mainly concentrated in the log-law layer, while the other layers are not shown in this paper because they are less affected by the Reynolds numbers. The comparison of figure 9(*c*,*d*) shows that at large scales, the spatial and interscale turbulent convections (T^{SP} and T^{SS}) are far smaller under larger Reynolds numbers. For these turbulent convections, smaller rotation numbers and larger Reynolds numbers have similar effects, as shown by the comparison of figure 9(*a*,*c*,*d*). In addition, Π^S and E^S are larger with a higher Reynolds number, as the turbulence is strengthened. Strictly speaking, the layer $x_2^+ \approx 80$ with $Re_\tau = 180$ does not fully scale in viscous units and is located at the junction between the inner and outer layers. If larger Reynolds numbers are considered, then these results may be invariant with respect to the Reynolds number, similar to those in the viscous sublayer and the buffer layer.

In conclusion, rotation extracts more energy from the buffer layer to other layers. In the viscous sublayer the turbulence intensity is mainly strengthened by the movement of the production peak and the intensive spatial viscous diffusion. In the log-law layer the turbulence is mainly strengthened by the spatial turbulent convection, the inhibited forward cascades and the thus weaker pseudo-dissipation. In fact, in homogeneous rotating turbulence (Mininni *et al.* 2009), forward cascade inhibition has also been confirmed, attributed to the decay of non-resonant interactions. In streamwise-rotating channel turbulence the structures in the log-low layer are strongly elongated by rotation. In contrast, those structures under the buffer layer are shortened. This could be attributed to the strongly inclined structures near the wall, which will be investigated in § 4. Furthermore, increasing Reynolds numbers result in weaker spatial turbulent convection and stronger interscale transfers, which is opposite to the rotation effects. This is associated with the relative importance between inertial motions and the rotation effects. Similarly, in homogeneous rotating turbulence, under rapid rotation ($\varOmega \rightarrow \infty$), the nonlinear turbulent convection is negligible (Davidson 2013).

4. Inclined structures and sustaining mechanisms

In § 3.1 it has been found that the inclination angles of large- and small-scale structures are completely different, and the difference is more remarkable as rotation becomes stronger. In this section we use the angle based on the velocity vector and the filtering approach to identify these inclined structures more quantitatively. Then, based on the related budget balance of the Reynolds stresses and AGKE for the second-order structure functions, we identify the key sustaining mechanisms for small-scale inclined structures, with further physical explanations provided through the hairpin vortex model. Finally, the scale discrepancy will also be discussed in detail.

4.1. *Identification of the inclined structures*

To confirm these observations about the inclined structures, figure 10 shows the vortex structures under the log-law layer ($x_2^+ < 90$) for the cases (*a*) ST00, (*b*) ST07 and (*c*) ST30. The structures are coloured by the distance from the wall and are shown with $Q > 500$, where $Q = [2|\nabla \times \boldsymbol{u}|^2 - |\nabla \boldsymbol{u} + (\nabla \boldsymbol{u})^T|^2]/8$. The white solid lines in (*b*) and (*c*) are given for reference of the inclination angles. As shown, the structures of ST07 and ST30 have larger lateral sizes than those of ST00, in agreement with the observation in figure 4(*c*). Furthermore, in figure 10(*a*) the structures of ST00 are fully aligned with the streamwise direction in all layers, where no rotation is introduced. The structures of ST07 are shown in figure 10(*b*). The structures have a small inclination angle (8.0°). Figure 10(*c*) gives the results for ST30. Most small-scale structures ($\Delta x_1^+ < 500$) have an angle of 16.0°. However, the large-scale structures ($\Delta x_1^+ > 2000$) display angles between 2.63° and 16.0°. In what follows, these structures will be identified by a more quantitative method.

For channel turbulence, researchers (Kim & Moin 1986; Jiménez 2011) usually use the velocity direction to recognize sweeps and ejections. Therefore, the inclination angle can be defined by the velocity field as

$$\theta_u = \tan^{-1}\{u_3/u_1\}. \tag{4.1}$$

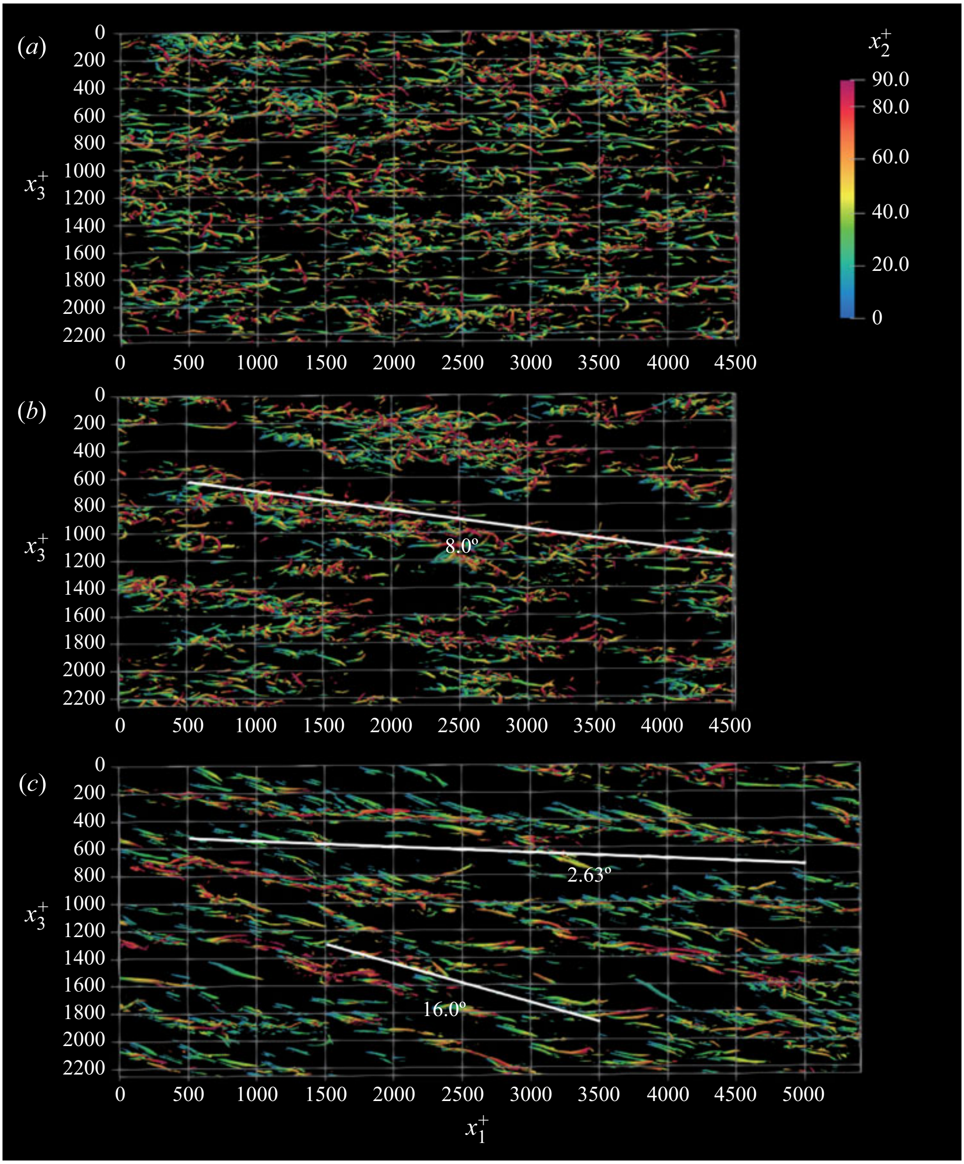

Figure 10. Flow structures under the log-law layer ($x_2^+ < 90$) with $Q > 500$ for the cases (*a*) ST00, (*b*) ST07, (*c*) ST30. The structure is coloured by x_2^+, with the colour bar on the right of panel (*a*). The white lines and labels are given for reference.

To illustrate the scale discrepancy, filtering methods are used to isolate the large- and small-scale results. The large- and small-scale angles are defined as

$$\theta_{u,L}(\boldsymbol{x}) = \tan^{-1}\left\{\frac{\displaystyle\int G_L(\boldsymbol{r})u_3(\boldsymbol{x}-\boldsymbol{r})\,\mathrm{d}\boldsymbol{r}}{\displaystyle\int G_L(\boldsymbol{r})u_1(\boldsymbol{x}-\boldsymbol{r})\,\mathrm{d}\boldsymbol{r}}\right\}, \quad \theta_{u,S}(\boldsymbol{x}) = \tan^{-1}\left\{\frac{\displaystyle\int G_S(\boldsymbol{r})u_3(\boldsymbol{x}-\boldsymbol{r})\,\mathrm{d}\boldsymbol{r}}{\displaystyle\int G_S(\boldsymbol{r})u_1(\boldsymbol{x}-\boldsymbol{r})\,\mathrm{d}\boldsymbol{r}}\right\}, \tag{4.2a,b}$$

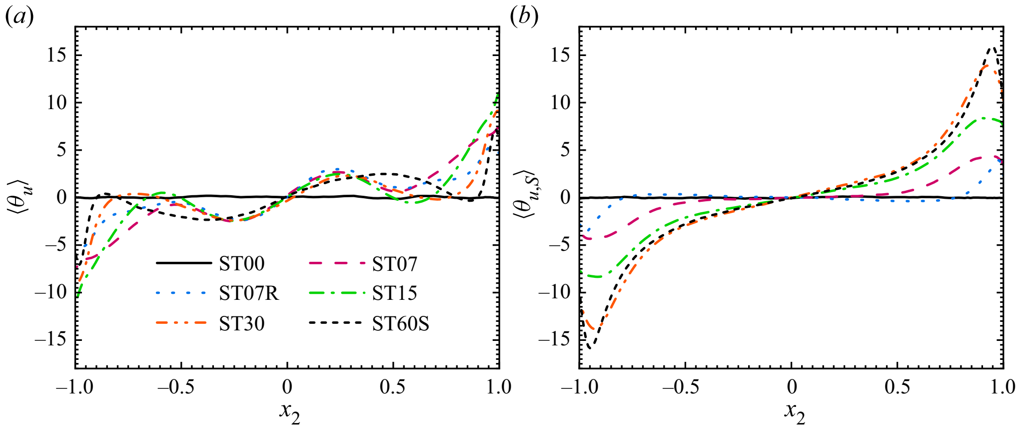

Figure 11. Comparison of the average inclination angles of different scales. (*a*) Average inclination angle $\langle\theta_u\rangle$. (*b*) Average inclination angle at small scales $\langle\theta_{u,S}\rangle$.

where G_L and G_S are corresponding filters. To avoid any artificial effects on the vortex direction, the same filter width is used in the streamwise and spanwise directions. Three filters and three filter widths are considered in Appendix B. Although affected by filters, the small-scale results manifest the same tendency. The large-scale results exhibit a similar distribution to the non-filtered results but are sensitive to the filter width. In our study, $\Delta_L \in [0.1\pi, 0.4\pi]$ and is comparable to the width of two-layer TGL vortices (0.16π). The TGL vortices have been studied by many researchers (Yang & Wang 2018) and are not the subject of this paper. In the following analysis, only the small-scale results with the Gaussian filters ((B1)) of $\Delta_S = 0.025\pi$ are presented.

The results are given in figure 11. As shown in figure 11(*a*), in the low log-law layer ($x_2^+ \approx 40$ and $x_2 \approx \pm 0.75$), as rotation becomes stronger, the average large-scale inclination angle $\langle\theta_{u,L}\rangle$ decreases. However, in the vicinity of the wall and around the channel centre, $\langle\theta_{u,L}\rangle$ is roughly unchanged for different cases. This should be attributed to the local distribution of a large-scale streamwise vortex, which is the limit of the inclination angle based on the velocity vector. However, the average small-scale angle $\langle\theta_{u,S}\rangle$ has completely different distributions, as shown in figure 11(*b*). As rotation intensifies, $\langle\theta_{u,S}\rangle$ near the wall ($x_2^+ \approx 18$ and $x_2 \approx \pm 0.1$) monotonically increases. In higher layers the $\langle\theta_{u,S}\rangle$ of ST60S is slightly smaller than that of ST30. Generally, this is consistent with the results shown in figure 6. There are also small differences, such as the specific values of angles, which can be attributed to their different definitions. Moreover, as Re_τ increases, $\langle\theta_{u,S}\rangle$ generally decreases. There could be two reasons. First, ST07R has a wider scale range, and the smallest scale is not affected by rotation, which is supported by the scale energy not shown. The second reason is the thinner boundary layer in ST07R. There is no inclination angle in homogeneous rotating turbulence. Roughly speaking, the inclined structures originate from the coupling effects of boundary layers and rotation. Case ST07R has a thinner boundary layer than ST07 and, thus, has a weaker inclination angle. This deduction can be verified by the fact that in figure 11 the $\langle\theta_{u,S}\rangle$ of ST07 and that of ST07R are almost the same under the viscous sublayer but are completely different away from the wall. Figure 12 shows the probability density function (PDF) of the small-scale inclination angle $\theta_{u,S}$ in (*a*) the buffer layer and (*b*) the low log-law layer. As rotation intensifies, the peaks of the PDF move toward a positive value. Furthermore, in the low

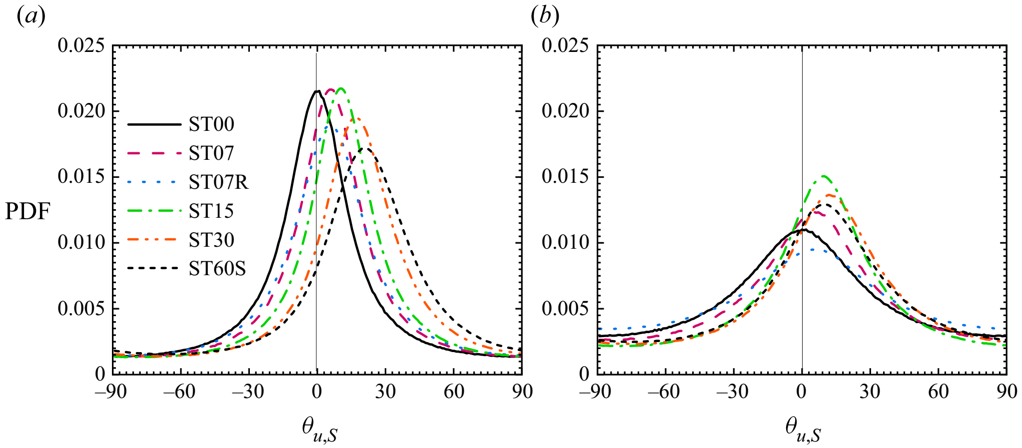

Figure 12. Comparison of the PDF of the small-scale inclination angle $\theta_{u,S}$ in (*a*) the buffer layer ($x_2^+ = 10.3$ for ST07R and $x_2^+ = 10.5$ for other cases) and (*b*) the low log-law layer ($x_2^+ = 46.6$ for all cases).

log-law layer, the peaks have weaker amplitudes than those in the buffer layer, indicating an isotropic tendency away from the wall.

4.2. *Sustaining mechanisms of the inclined structures*

After the identification of the inclined structures, the focus is on the sustaining mechanisms of these structures. Since the distribution of $\langle u_1 u_3 \rangle$ is similar to that of $\langle \theta_u \rangle$, for simplification, the phenomena are analysed based on the budget balance of $\langle u_1 u_3 \rangle$ and the AGKE of $\langle \delta u_1 \delta u_3 \rangle$. For an overview of the mechanisms, the Reynolds stress budget equation is studied first and is written as

$$\underbrace{-\langle u_2 u_j \rangle \frac{\mathrm{d}\langle U_i \rangle}{\mathrm{d}x_2} - \langle u_2 u_i \rangle \frac{\mathrm{d}\langle U_j \rangle}{\mathrm{d}x_2}}_{\Pi_{ij}} \underbrace{+ 2\Omega \langle \epsilon_{1im} u_j u_m + \epsilon_{1jm} u_i u_m \rangle}_{C_{ij}} \underbrace{- \frac{\mathrm{d}}{\mathrm{d}x_2} \langle u_i u_j u_2 \rangle}_{T_{ij}}$$

$$\underbrace{- \frac{1}{\rho} \left\langle u_j \frac{\partial p_R}{\partial x_i} + u_i \frac{\partial p_R}{\partial x_j} \right\rangle}_{P_{R,ij}} \underbrace{- \frac{1}{\rho} \left\langle u_j \frac{\partial p_T}{\partial x_i} + u_i \frac{\partial p_T}{\partial x_j} \right\rangle}_{P_{T,ij}}$$

$$\underbrace{+ \nu \frac{\mathrm{d}^2}{\mathrm{d}x_2^2} \langle u_i u_j \rangle}_{D_{ij}} \underbrace{- 2\nu \left\langle \frac{\partial u_i}{\partial x_k} \frac{\partial u_j}{\partial x_k} \right\rangle}_{-E_{ij}} = 0, \tag{4.3}$$

where Π_{ij} is the production, C_{ij} is the Coriolis term, T_{ij} is the turbulent convection, D_{ij} is the viscous diffusion, E_{ij} is the pseudo-dissipation, and $P_{R,ij}$ and $P_{T,ij}$ are the pressure–velocity correlation terms related to the rotation effects and turbulent convection, respectively. Since C_{ij} and $P_{R,ij}$ are both induced by rotation and are strongly cancelled by each other, the two terms are summed to form a new term $C_{ij,eff}$ (Yang *et al.* 2020*a*).

The budget balance for the Reynolds stresses ($\langle u_1 u_3 \rangle$ and $\langle u_2 u_3 \rangle$) of ST30 is given in figure 13. The terms in figure 13 have opposite signs to those reported by Yang

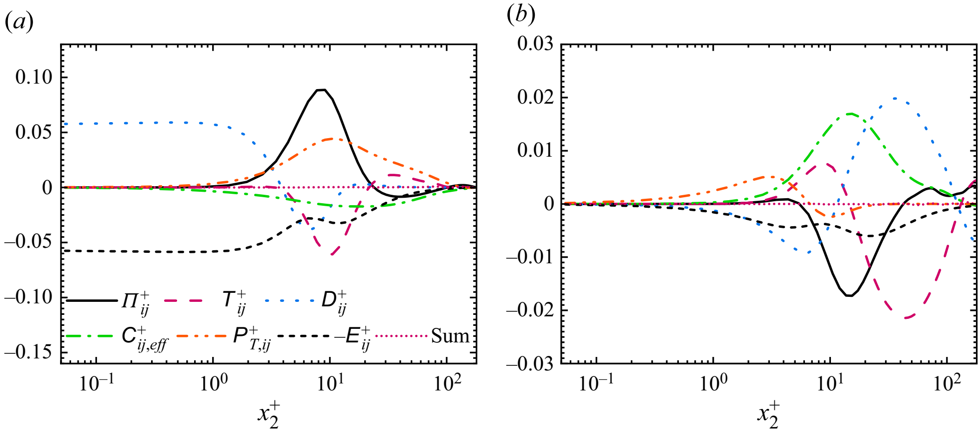

Figure 13. Budget balance of $\langle u_iu_j\rangle^+$ for ST30: (*a*) $\langle u_1u_3\rangle^+$, (*b*) $\langle u_2u_3\rangle^+$.

& Wang (2018) due to the different domain ranges evaluated. Specifically, this study examines the upper domain ($x_2 \in [0, 1]$), while Yang & Wang (2018) explored the lower domain ($x_2 \in [-1, 0]$). As shown in figure 13(*a*), the effective Coriolis term $C_{13,eff}$ reduces the inclination angle. In contrast, there are two main sources for $\langle u_1u_3\rangle$, i.e. the convection-induced pressure–velocity correlation term $P_{T,13}$ and the production Π_{13}. $P_{T,ij}$ can be simplified as

$$P_{T,ij} = -\frac{1}{\rho}\left\langle u_i\frac{\partial p_T}{\partial x_j} + u_j\frac{\partial p_T}{\partial x_i}\right\rangle = -\frac{1}{\rho}\left\langle \frac{\partial u_ip_T}{\partial x_j} + \frac{\partial u_jp_T}{\partial x_i}\right\rangle + \frac{2}{\rho}\langle p_TS_{ij}\rangle, \tag{4.4}$$

where the strain rate tensor $S_{ij} = (\partial u_i/\partial x_j + \partial u_j/\partial x_i)/2$. Here, $P_{T,13} = 2\langle p_TS_{13}\rangle/\rho$ and could be related to the strain rate tensor. To confirm the effect of the strain, the principal directions of the strain rate tensors ($\langle\theta_{S_{ij}}\rangle$ and $\langle\theta_{S_{ij},S}\rangle$) are calculated by the eigenvector with $\max\{|\lambda_i|\}$, where λ_i is the eigenvalue. The principal directions of the strain rate tensors are given in figure 14. As shown, the tendency of $\langle\theta_{S_{ij},S}\rangle$ is similar to that of $\langle\theta_{u,S}\rangle$ in figure 11. On the one hand, the strain tries to induce these inclined structures via $P_{T,13}$. On the other hand, the strain also affects the dissipation, which reduces the inclination angle. Another more important source is the production Π_{13}, which can be decomposed into two components ($\Pi_{13,1}$ and $\Pi_{13,2}$), i.e.,

$$\Pi_{13} = \underbrace{-\langle u_2u_3\rangle\frac{\mathrm{d}\langle U_1\rangle}{\mathrm{d}x_2}}_{\Pi_{13,1}}\underbrace{-\langle u_1u_2\rangle\frac{\mathrm{d}\langle U_3\rangle}{\mathrm{d}x_2}}_{\Pi_{13,2}}. \tag{4.5}$$

Figure 15 gives (*a*) the production and (*b*,*c*) its decomposition. The production Π_{13} is the main reason for the inclination angle. It is positive in the buffer layer but negative in higher layers. As rotation intensifies, the positive peak moves towards the wall and has a larger value. The decomposition in figure 15(*b*,*c*) shows that $\Pi_{13,1}$ is responsible for the positive peaks, especially for strongly rotating cases (ST30 and ST60S). Here, $\Pi_{13,1}$ originates from the Reynolds stress $\langle u_2u_3\rangle$. As shown in figure 13(*b*), the effective Coriolis term $C_{23,eff}$ is the only source for positive $\langle u_2u_3\rangle$. In other words, $C_{23,eff}$ induces positive $\langle u_2u_3\rangle$, and then, under the strain induced by $\langle U_1\rangle$, $\langle u_2u_3\rangle$ further leads to these inclined structures. Notably, Yang *et al.* (2020*a*) found that $\langle u_2u_3\rangle$ constrains itself from increasing

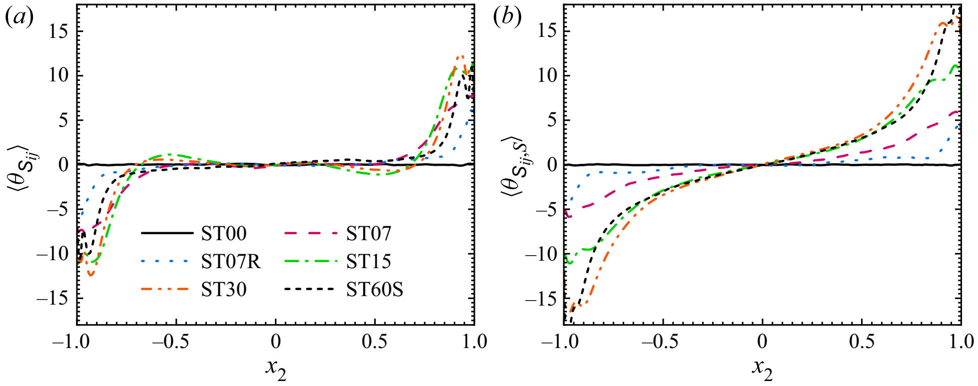

Figure 14. Comparison of the average inclination angles given by the principal directions of the strain rate tensor. (*a*) Average inclination angle $\langle \theta_{S_{ij}} \rangle$. (*b*) Average inclination angle at small scales $\langle \theta_{S_{ij},S} \rangle$.

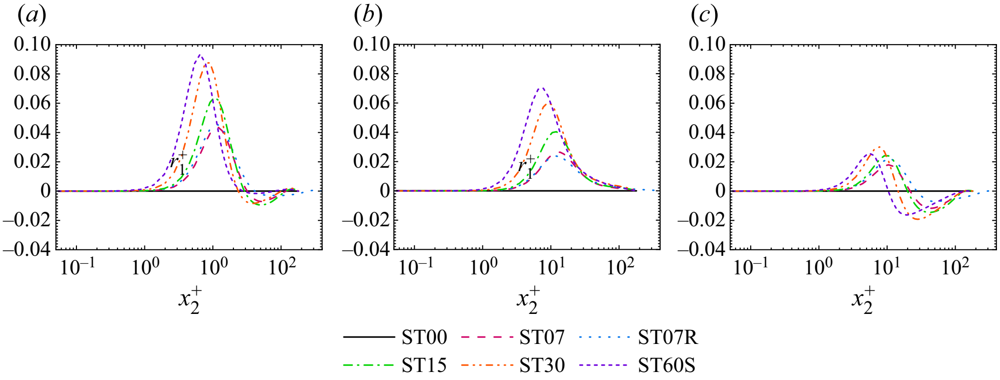

Figure 15. Production decomposition for the budget balance of $\langle u_1u_3 \rangle^+$. Results are shown for (*a*) Π_{13}^+, (*b*) $\Pi_{13,1}^+$, (*c*) $\Pi_{13,2}^+$.

infinitely. From $\Pi_{13,1}$, it can be inferred that with stronger rotation, the inclination angle also cannot infinitely increase, as confirmed by the $\langle \theta_{u,S} \rangle$ of ST30 and ST60S in figure 11.

To illustrate how these strongly inclined small-scale structures are sustained under rotation, a simple hairpin vortex model is proposed here. To be consistent with the previous analysis, the upper channel domain ($x_2 \in [0, 1]$) is considered. It is in a left-handed coordinate system because a transform of $x_2 \leftarrow 1 - x_2$ is used when the upper domain is discussed. For a clearer illustration, the three main effects can be summarized as

$$\left.\begin{aligned} \Pi_{13,1} &= \left\langle u_3 \left(-u_2 \frac{\mathrm{d}\langle U_1 \rangle}{\mathrm{d}x_2} \right) \right\rangle = \langle u_3 F_{\Pi 1} \rangle \quad \text{for} \left\langle u_3 \frac{\partial u_1}{\partial t} \right\rangle, \\ C_{23} &\approx \langle u_3(2\Omega u_3) \rangle = \langle u_3 F_{C2} \rangle \quad \text{for} \left\langle u_3 \frac{\partial u_2}{\partial t} \right\rangle, \\ C_{13} &= \langle u_1(-2\Omega u_2) \rangle = \langle u_1 F_{C3} \rangle \quad \text{for} \left\langle u_1 \frac{\partial u_3}{\partial t} \right\rangle, \end{aligned}\right\} \tag{4.6}$$

where $-2\Omega \langle u_2u_2 \rangle$ in C_{23} is negligible compared with $2\Omega \langle u_3u_3 \rangle$. In (4.6), $F_{\Pi 1}$, F_{C2}, and F_{C3} are the corresponding forces of the three key terms $\Pi_{13,1}$, C_{23} and C_{13}, respectively.

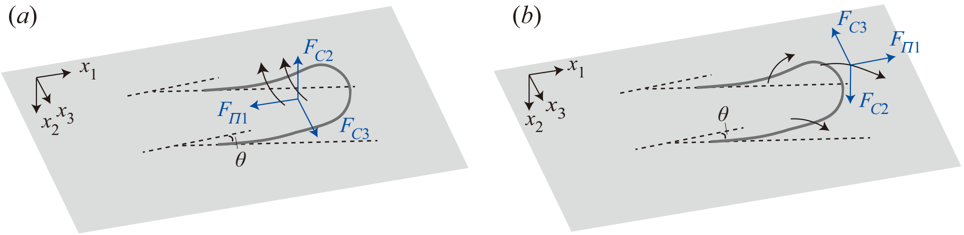

Figure 16. Three forces in the (*a*) ejection and (*b*) sweep of a hairpin vortex. The upper half-domain is given to be consistent with the above analysis, and thus, the left-handed system is used. The black arrows give the main region of ejections and sweeps, and the dark blue arrows show the force directions.

The forces directly affect the momentum and, thus, the Reynolds stresses $\langle u_1 u_3 \rangle$ and $\langle u_2 u_3 \rangle$. The analysis of the three forces on a vortex could give some intuitions about the mechanisms shown by the Reynolds stress budget balance. In figure 16 two events of a hairpin vortex are considered: (*a*) ejections with $\{u_1 < 0, u_2 < 0, u_3 < 0\}$ and (*b*) sweeps with $\{u_1 > 0, u_2 > 0, u_3 > 0\}$. As shown by the black arrows, fluid ejects mainly in the inboard of the vortex and sweeps mainly in the outboard region (Adrian 2007). The assumption of u_1 and u_2 is based on the ejection and sweep models of the hairpin vortex (Jiménez 2011). The models are still effective in streamwise-rotating channel turbulence because the distribution of $\langle u_1 u_2 \rangle$ is almost unaffected by the streamwise rotation (Yang & Wang 2018), and hairpin vortexes are also observed in ST07 in figure 10. Notably, contrary to the classical hairpin vortex model, since the upper domain is considered here, $u_2 < 0$ for the ejections and $u_2 > 0$ for the sweeps. In addition, due to $\langle \theta_{u,S} \rangle$ in figure 11, u_3 is selected to have the same sign as u_1. Based on the hairpin vortex model in figure 16, the effects of the forces on the ejection and sweep are illustrated separately.

(i) As shown in figure 16(*a*), in the ejection, the Coriolis force F_{C3} tries to induce a positive spanwise velocity u_3, which is opposite to the assumption $u_3 < 0$. Since $u_1 < 0$, $u_1 F_{C3} < 0$. This is consistent with the negative term $\mathcal{C}_{13,eff}$ in figure 13(*a*) and is the direct mechanism of $\mathcal{C}_{13,eff}$ reducing the positive inclination angle. In contrast, since $u_3 < 0$, F_{C2} tries to induce negative u_2, consistent with the ejection assumption of $u_2 < 0$. Then, as $u_2 < 0$, $F_{\Pi 1}$ related to $\Pi_{13,1}$ tries to induce negative u_1, and thus, $u_3 F_{\Pi 1} > 0$. The effects of the forces F_{C2} and $F_{\Pi 1}$ are consistent with the budget balance of $\langle u_2 u_3 \rangle$ and $\langle u_1 u_3 \rangle$. This mechanism is responsible for the small-scale inclined structures near the wall. Here F_{C2} strengthens the wall-normal velocity and $F_{\Pi 1}$, which further induces the inclination structures.

(ii) As shown in figure 16(*b*), in the sweep, F_{C3} leads to a negative spanwise velocity u_3 and $u_1 F_{C3} < 0$, which reduces the positive inclination angle; F_{C2} tries to induce positive u_2; $F_{\Pi 1}$ intensifies the positive u_1, and thus, $u_3 F_{\Pi 1} > 0$. The effects of the three forces are also consistent with the budget balance of $\langle u_2 u_3 \rangle$ and $\langle u_1 u_3 \rangle$.

Through this hairpin vortex model, the physical processes hidden under the Reynolds stress budget balance are clearly shown. In conclusion, there are two main mechanisms. First, $\mathcal{C}_{13}$ related to F_{C3} directly reduces the inclination angle. In contrast, $\mathcal{C}_{23}$ related to F_{C2} indirectly induces a positive $\langle u_2 u_3 \rangle$, which then results in inclination structures under the mean shear stress induced by $\Pi_{13,1}$.

To further confirm the findings, the scale decompositions are considered using the AGKE, which was deduced by Gatti *et al.* (2020) for inhomogeneous turbulence.

In channel turbulence with streamwise rotation, the AGKE is written as

$$
\begin{aligned}
0 = {} & \underbrace{-\langle\delta u_j\delta u_2\rangle\left\langle\frac{\partial U_i}{\partial X_2}\right\rangle^* - \langle\delta u_i\delta u_2\rangle\left\langle\frac{\partial U_j}{\partial X_2}\right\rangle^*}_{\Pi^S_{ij}} + \underbrace{2\Omega(\varepsilon_{1im}\langle\delta u_j\delta u_m\rangle + \varepsilon_{1jm}\langle\delta u_i\delta u_m\rangle)}_{C^S_{ij}} \\
& \underbrace{-\frac{\partial}{\partial X_2}\langle\delta u_i\delta u_j u_2^*\rangle}_{T^{SP}_{ij}} \underbrace{-\frac{\partial}{\partial r_k}\langle\delta u_i\delta u_j\delta u_k\rangle}_{T^{SS}_{ij}} \underbrace{-\frac{1}{\rho}\left\langle\delta u_j\frac{\partial\delta p_R}{\partial X_i} + \delta u_i\frac{\partial\delta p_R}{\partial X_j}\right\rangle}_{P^S_{R,ij}} \\
& \underbrace{-\frac{1}{\rho}\left\langle\delta u_j\frac{\partial\delta p_T}{\partial X_i} + \delta u_i\frac{\partial\delta p_T}{\partial X_j}\right\rangle}_{P^S_{T,ij}} + \underbrace{\frac{\nu}{2}\frac{\partial^2}{\partial X_2^2}\langle\delta u_i\delta u_j\rangle}_{D^{SP}_{ij}} + \underbrace{2\nu\frac{\partial^2}{\partial r_k\partial r_k}\langle\delta u_i\delta u_j\rangle}_{D^{SS}_{ij}} \underbrace{-4\langle\epsilon_{ij}\rangle^*}_{-E^S_{ij}},
\end{aligned}
\tag{4.7}
$$

where T^{SS}_{ij} and T^{SP}_{ij} are the turbulent convections in scale and spatial space, Π^S_{ij} is the production, $P^S_{ij,R}$ and $P^S_{ij,T}$ are the pressure–velocity correlation terms induced by rotation and convection, D^{SS}_{ij} and D^{SP}_{ij} are the interscale and spatial viscous diffusion, E^S_{ij} is the pseudo-dissipation and $\epsilon_{ij} = \nu(\partial u_i/\partial x_k)(\partial u_j/\partial x_k)$. Figure 17 shows the AGKE of $\langle\delta u_1\delta u_3\rangle$ for ST30 in the buffer layer ($x_2^+ = 10.5$). The main conclusion is consistent with that obtained based on the budget balance of $\langle u_1u_3\rangle$. Therefore, it is reliable to use the budget balance of $\langle u_1u_3\rangle$ to study the mechanisms for small-scale inclined structures. Furthermore, at small scales, there are still positive interscale turbulent convection T^{SS}_{13} and interscale viscous diffusion D^{SS}_{13}, similar to the GKE results in figure 8. These strongly inclined structures are produced around $r_1^+ \approx 100$ and then induce inclined structures at smaller scales via forward cascades.

Finally, the mechanisms underlying the discrepancy between small- and large-scale inclination angles observed based on $\langle\theta_u\rangle$ and $\langle\theta_{u,S}\rangle$ are investigated. As shown in figure 11, in the low log-law layer ($x_2^+ = 46.6$), as Ro_τ increases from 0 to 30, the structures of overall scale have weaker inclination angles, but small-scale structures have stronger angles. According to the production decomposition in figure 15, the decaying angles for large-scale structures could be mainly attributed to the negative $\Pi_{13,2}$ in the log-law layer. According to the profile in figure 2 and the Reynolds stresses given by Yang & Wang (2018), in the boundary layer, $\langle u_1u_2\rangle$ does not change its sign, while the behaviour is the opposite for $\partial\langle U_3\rangle/\partial x_2$. Therefore, the mean spanwise velocity gradients could be responsible for the decaying angles of large-scale structures with increasing rotation rates. To further confirm the deduction, the production in the AGKE is also decomposed as follows:

$$
\Pi^S_{13} = \underbrace{-\langle\delta u_3\delta u_2\rangle\left\langle\frac{\partial U_1}{\partial X_2}\right\rangle^*}_{\Pi^S_{13,1}} \underbrace{-\langle\delta u_1\delta u_2\rangle\left\langle\frac{\partial U_3}{\partial X_2}\right\rangle^*}_{\Pi^S_{13,2}}. \tag{4.8}
$$

Figure 18 shows the decomposition for ST30 at $x_2^+ = 46.6$, where panel (*a*) gives the overall production Π^{S+}_{13} and panels (*b*,*c*) give the decomposition. As shown in figure 18(*a*), for ST30 and ST60S with strong scale discrepancies, Π^S_{13} is positive at small scales but negative at large scales. For ST07 with no obvious discrepancy, the production is

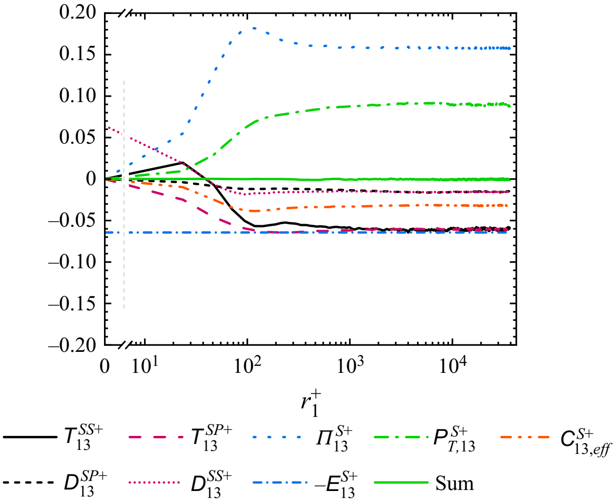

Figure 17. The AGKE of $\langle \delta u_1 \delta u_3 \rangle^+$ for ST30 in the buffer layer ($x_2^+ = 10.5$).

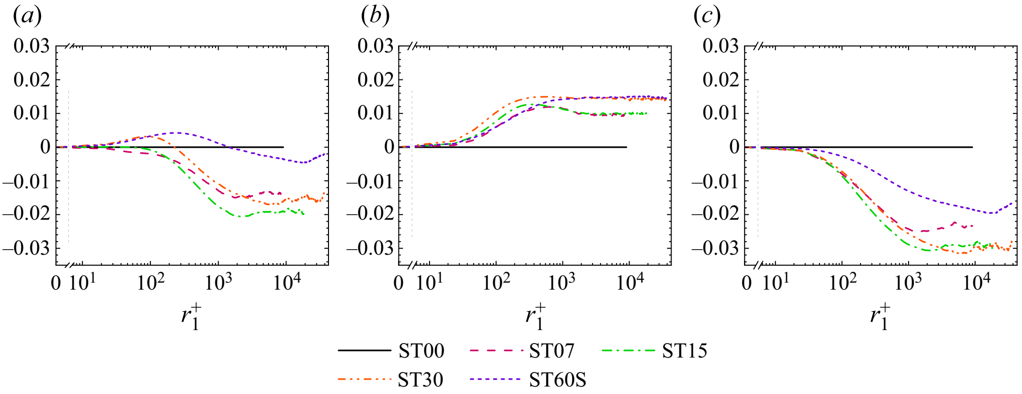

Figure 18. Decomposition of the production in the AGKE of $\langle \delta u_1 \delta u_3 \rangle^+$ in the low log-law layer ($x_2^+ = 46.6$). Results are shown for (*a*) Π_{13}^{S+}, (*b*) $\Pi_{13,1}^{S+}$, (*c*) $\Pi_{13,2}^{S+}$.

completely negative. As shown by the decomposition in figure 18(*b*,*c*), $\Pi_{13,1}^{S+}$ is always positive, and the behaviour is the opposite for $\Pi_{13,2}^{S+}$. Therefore, the scale discrepancy arises mainly because large-scale inclined structures are more sensitive to the mean spanwise velocity gradients.

5. Conclusion

Streamwise-rotating channel turbulence is a typical multiscale and inhomogeneous flow. In this paper, based on basic turbulence statistics, second-order structure functions and their budget balance, we have investigated the multiscale dynamics in streamwise-rotating channel turbulence.

Seven DNS are taken into consideration. The Reynolds number is 180 or 395, and the rotation number ranges from 0 to 60. Through the TKE budget balance, we find that under rotation, the near-wall turbulence is strengthened, which is mainly related to the spanwise TKE $\langle u_3u_3\rangle$. In addition, the pseudo-dissipation above the buffer layer is reduced by rotation. To further investigate the spatial and interscale dynamics, the GKE is introduced. First, we study the distribution of the scale energy and find that small- and large-scale structures have different inclination angles in rapidly rotating cases. Additionally, we find that rotation shortens the streamwise structures in the viscous sublayer and buffer layer, which could be attributed to the strongly inclined small-scale structures near the wall. In contrast, the streamwise structures above the buffer layer are elongated by rotation. Then, we analyse the transfer of the scale energy utilizing the GKE. We discover that rotation strengthens the turbulence intensity in the viscous sublayer, mainly through the variation of the production distribution and the spatial viscous diffusion. In the buffer layer the pseudo-dissipation and interscale transfers at small scales are suppressed by rotation. At large scales, the turbulent interscale and spatial transfers are both strengthened. In the log-law layer, rotation destroys the spatial local balance and suppresses the pseudo-dissipation. The phenomenon of the reduced pseudo-dissipation is related to the suppressed forward cascades induced by rotation and has also been found in homogeneous rotating turbulence. We also find the opposite effects between the Reynolds and rotation numbers on the interscale transfers.

Finally, based on the filtered velocity field, we quantitatively investigate the large- and small-scale inclined structures. Large- and small-scale structures have different inclination angles. As rotation intensifies, the difference becomes more remarkable. As Re_τ becomes larger, the inclination angle is generally reduced due to the wider scale range and the thinner boundary layer. Then, the sustaining mechanisms of inclined structures are analysed based on the budget balance of the Reynolds stresses and AGKE of $\langle\delta u_1\delta u_3\rangle$. We find that the Coriolis force directly reduces the inclination angle. In contrast, the pressure–velocity correlation term arises from inclined structures and can be related to the principal direction of the strain rate tensor. Indirectly, the Coriolis force induces non-zero $\langle u_2u_3\rangle$, which then produces inclined structures under the mean streamwise velocity gradients. We then clearly illustrate the direct and indirect effects of the Coriolis forces through the hairpin vortex model, which provides insight into the physical processes hidden behind the complex turbulence statistics. The scale discrepancies in the inclined structures are mainly attributed to the mean spanwise velocity gradients.

In conclusion, through detailed and systematic analyses, we have investigated the multiscale dynamics in streamwise-rotating channel turbulence. The specific energy transfer behaviours, new features of the structures and their sustaining mechanisms have been identified and analysed in this paper. We expect this study to help in exploring the rotation effects in general wall-bounded turbulent flows.

Funding. This work was supported by the National Key Research and Development Program of China (grant nos. 2019YFA0405300 and 2020YFA0711800) and NSFC Projects (grant nos. 12072349, 12232018, 91852203 and 12202457).

Declaration of interests. The authors report no conflict of interest.

Author ORCIDs.
Running Hu https://orcid.org/0000-0002-3423-5583;
Changping Yu https://orcid.org/0000-0002-2126-1344.

Appendix A. Two-point correlations and high-precision post-processing

According to the relationships among the partial derivatives (Hill 2002)

$$\left.\begin{aligned} \frac{\partial}{\partial x_i} &= \frac{\partial}{\partial r_i} + \frac{1}{2}\frac{\partial}{\partial X_i}, \quad & \frac{\partial}{\partial x'_i} &= -\frac{\partial}{\partial r_i} + \frac{1}{2}\frac{\partial}{\partial X_i}, \\ \frac{\partial}{\partial X_i} &= \frac{\partial}{\partial x_i} + \frac{\partial}{\partial x'_i}, \quad & \frac{\partial}{\partial r_i} &= \frac{1}{2}\left(\frac{\partial}{\partial x_i} - \frac{\partial}{\partial x'_i}\right), \end{aligned}\right\} \tag{A1}$$

all the terms of the GKE in (3.3) can be written as follows.

The time derivative term is

$$\frac{1}{2}\frac{\partial \langle \delta u^2\rangle}{\partial t} = \frac{\partial}{\partial t}\langle (u_i u_i)^* - u_i u'_i\rangle. \tag{A2}$$

The interscale turbulent convection can be written as

$$\begin{aligned} -\frac{1}{2}\frac{\partial}{\partial r_{\underline{j}}}\langle \delta u^2 \delta u_{\underline{j}}\rangle = {} & \frac{1}{4}\left[-\left\langle \frac{\partial}{\partial x_{\underline{j}}} u_i u_i u_{\underline{j}}\right\rangle - \left\langle u'_i u'_i \frac{\partial}{\partial x_{\underline{j}}} u_{\underline{j}}\right\rangle + 2\left\langle u'_i \frac{\partial}{\partial x_{\underline{j}}} u_i u_{\underline{j}}\right\rangle \right. \\ & \left. + \left\langle u'_{\underline{j}} \frac{\partial}{\partial x_{\underline{j}}} u_i u_i\right\rangle - 2\left\langle u'_i u'_{\underline{j}} \frac{\partial}{\partial x_{\underline{j}}} u_i\right\rangle\right] \\ & + \frac{1}{4}\left[-\left\langle \frac{\partial}{\partial x'_{\underline{j}}} u'_i u'_i u'_{\underline{j}}\right\rangle - \left\langle u_i u_i \frac{\partial}{\partial x'_{\underline{j}}} u'_{\underline{j}}\right\rangle + 2\left\langle u_i \frac{\partial}{\partial x'_{\underline{j}}} u'_i u'_{\underline{j}}\right\rangle \right. \\ & \left. + \left\langle u_{\underline{j}} \frac{\partial}{\partial x'_{\underline{j}}} u'_i u'_i\right\rangle - 2\left\langle u_i u_{\underline{j}} \frac{\partial}{\partial x'_{\underline{j}}} u'_i\right\rangle\right], \end{aligned} \tag{A3}$$

where the underline in the subscript represents no tensor contraction, and thus, the impressible constraint $\partial u_i/\partial x_i = 0$ cannot be applied.

The production can be written as

$$\begin{aligned} -\langle \delta u_1 \delta u_2\rangle \left\langle \frac{\partial U_1}{\partial x_2}\right\rangle^* - \langle \delta u_2 \delta u_3\rangle \left\langle \frac{\partial U_3}{\partial x_2}\right\rangle^* = {} & -\langle 2(u_1 u_2)^* - (u'_1 u_2 + u_1 u'_2)\rangle \left\langle \frac{\partial U_1}{\partial x_2}\right\rangle^* \\ & - \langle 2(u_2 u_3)^* - (u'_2 u_3 + u_2 u'_3)\rangle \left\langle \frac{\partial U_3}{\partial x_2}\right\rangle^*. \end{aligned} \tag{A4}$$

The spatial turbulent convection can be written as

$$\begin{aligned} -\frac{1}{2}\frac{\partial}{\partial X_2}\langle \delta u^2 u_2^*\rangle = {} & \frac{1}{4}\left[-\left\langle \frac{\partial}{\partial x_2} u_i u_i u_2\right\rangle - \left\langle u'_i u'_i \frac{\partial}{\partial x_2} u_2\right\rangle + 2\left\langle u'_i \frac{\partial}{\partial x_2} u_i u_2\right\rangle \right. \\ & \left. - \left\langle u'_2 \frac{\partial}{\partial x_2} u_i u_i\right\rangle + 2\left\langle u'_i u'_2 \frac{\partial}{\partial x_2} u_i\right\rangle\right] \\ & + \frac{1}{4}\left[-\left\langle \frac{\partial}{\partial x'_2} u'_i u'_i u'_2\right\rangle - \left\langle u_i u_i \frac{\partial}{\partial x'_2} u'_2\right\rangle + 2\left\langle u_i \frac{\partial}{\partial x'_2} u'_i u'_2\right\rangle \right. \\ & \left. - \left\langle u_2 \frac{\partial}{\partial x'_2} u'_i u'_i\right\rangle + 2\left\langle u_i u_2 \frac{\partial}{\partial x'_2} u'_i\right\rangle\right]. \end{aligned} \tag{A5}$$

The spatial rotation-induced pressure transport can be written as

$$
\begin{aligned}
-\frac{1}{\rho}\frac{\partial}{\partial X_2}\langle \delta u_2 \delta p^R\rangle &= \frac{1}{\rho}\left[-\left\langle \frac{\partial}{\partial x_2} u_2 p^R\right\rangle + \left\langle p^{R'}\frac{\partial}{\partial x_2}u_2\right\rangle + \left\langle u_2'\frac{\partial}{\partial x_2}p^R\right\rangle\right] \\
&\quad + \frac{1}{\rho}\left[-\left\langle\frac{\partial}{\partial x_2'}u_2'p^{R'}\right\rangle + \left\langle p^R \frac{\partial}{\partial x_2'}u_2'\right\rangle + \left\langle u_2\frac{\partial}{\partial x_2'}p^{R'}\right\rangle\right].
\end{aligned}
\tag{A6}
$$

The spatial convection-induced pressure transport can be written by replacing p^R with p^T.

The interscale viscous diffusion can be written as

$$
\begin{aligned}
\nu\frac{\partial^2}{\partial r_{\underline{j}}\partial r_{\underline{j}}}\langle \delta u^2\rangle &= \frac{\nu}{4}\left[\left\langle \frac{\partial^2 u_i u_i}{\partial x_{\underline{j}}\partial x_{\underline{j}}}\right\rangle - 2\left\langle u_i'\frac{\partial^2 u_i}{\partial x_{\underline{j}}\partial x_{\underline{j}}}\right\rangle\right] \\
&\quad + \frac{\nu}{4}\left[\left\langle \frac{\partial^2 u_i' u_i'}{\partial x_{\underline{j}}'\partial x_{\underline{j}}'}\right\rangle - 2\left\langle u_i\frac{\partial^2 u_i'}{\partial x_{\underline{j}}'\partial x_{\underline{j}}'}\right\rangle\right] + \nu\left\langle\frac{\partial u_i}{\partial x_{\underline{j}}}\frac{\partial u_i'}{\partial x_{\underline{j}}'}\right\rangle.
\end{aligned}
\tag{A7}
$$

The spatial viscous diffusion can be written as

$$
\begin{aligned}
\frac{\nu}{4}\frac{\partial^2}{\partial X_2^2}\langle \delta u^2\rangle &= \frac{\nu}{4}\left[\left\langle \frac{\partial^2 u_i u_i}{\partial x_2\partial x_2}\right\rangle - 2\left\langle u_i'\frac{\partial^2 u_i}{\partial x_2\partial x_2}\right\rangle\right] \\
&\quad + \frac{\nu}{4}\left[\left\langle \frac{\partial^2 u_i' u_i'}{\partial x_2'\partial x_2'}\right\rangle - 2\left\langle u_i\frac{\partial^2 u_i'}{\partial x_2'\partial x_2'}\right\rangle\right] - \nu\left\langle\frac{\partial u_i}{\partial x_2}\frac{\partial u_i'}{\partial x_2'}\right\rangle.
\end{aligned}
\tag{A8}
$$

The pseudo-dissipation is the same.

Appendix B. The effects of filters on the inclined angles

Three filters are considered here, including the Gaussian, box and sharp spectral filters.

The Gaussian filter can be written in the Fourier space as

$$
\left.
\begin{aligned}
\hat{G}_L(k_1, k_3) &= \exp(-(k_1^2 + k_3^2)\varDelta_L^2/24), \\
\hat{G}_S(k_1, k_3) &= 1 - \exp(-(k_1^2 + k_3^2)\varDelta_S^2/24),
\end{aligned}
\right\}
\tag{B1}
$$

where k_1 and k_3 are streamwise and spanwise wavenumbers, $\varDelta_L$ and $\varDelta_S$ are the filter widths for corresponding filters.

The box filter can be written in the Fourier space as

$$
\left.
\begin{aligned}
\hat{G}_L(k_1, k_3) &= \frac{\sin\left(\dfrac{1}{2}\sqrt{(k_1^2 + k_3^2)}\varDelta_L\right)}{\dfrac{1}{2}\sqrt{(k_1^2 + k_3^2)}\varDelta_L}, \\
\hat{G}_S(k_1, k_3) &= 1 - \frac{\sin\left(\dfrac{1}{2}\sqrt{(k_1^2 + k_3^2)}\varDelta_S\right)}{\dfrac{1}{2}\sqrt{(k_1^2 + k_3^2)}\varDelta_S}.
\end{aligned}
\right\}
\tag{B2}
$$

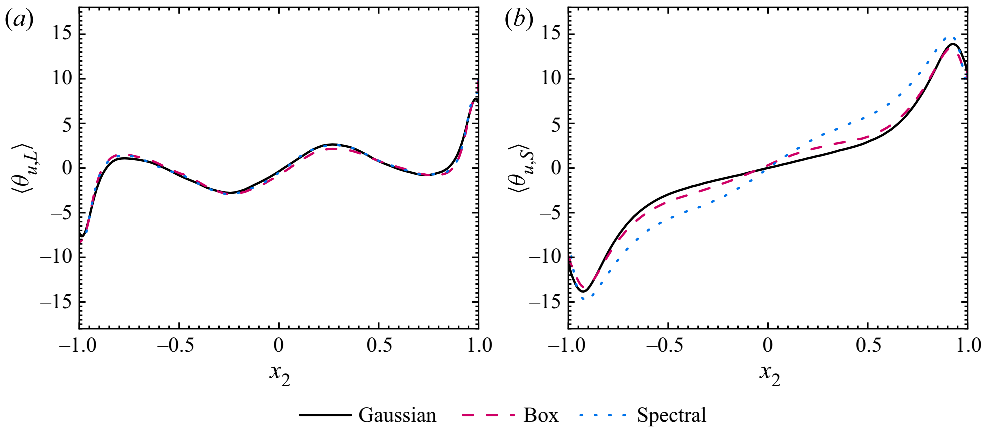

Figure 19. The filter effects on (*a*) $\langle\theta_{u,L}\rangle$ and (*b*) $\langle\theta_{u,S}\rangle$ of ST30.

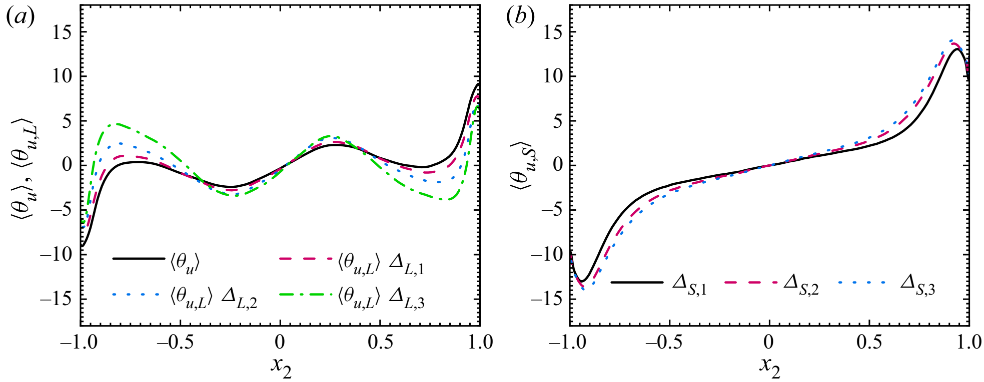

Figure 20. The filter width effects on (*a*) $\langle\theta_{u,L}\rangle$ and (*b*) $\langle\theta_{u,S}\rangle$ of ST30. For reference, $\langle\theta_u\rangle$ is given in panel (*a*).

The sharp spectral filter can be written in the Fourier space as

$$\left.\begin{aligned}\hat{G}_L(k_1,k_3) &= H\left(\frac{\pi}{\varDelta_L} - \left|\sqrt{(k_1^2+k_3^2)}\right|\right),\\ \hat{G}_S(k_1,k_3) &= H\left(-\frac{\pi}{\varDelta_S} + \left|\sqrt{(k_1^2+k_3^2)}\right|\right),\end{aligned}\right\} \tag{B3}$$

where $H(x)$ is the Heaviside function.

The effects of filters are shown in figure 19. As shown, the filters have no effect on the large-scale averaged inclined angle but affect the small-scale averaged inclination angle. Nonetheless, the small-scale results exhibit the consistent trend regardless of the filters used.

The effects of the filter widths are shown in figure 20, where $\varDelta_{L,i} = \{0.1\pi, 0.2\pi, 0.4\pi\}$, $\varDelta_{S,i} = \{0.05\pi, 0.025\pi, 0.0125\pi\}$ and $i = \{1, 2, 3\}$. As shown, $\langle\theta_{u,L}\rangle$ has similar distributions with $\langle\theta_u\rangle$, and is strongly affected by filter widths. In contrast, $\langle\theta_{u,S}\rangle$ is approximately independent of filter widths and is related to the main subjects of this paper.

REFERENCES

ADRIAN, R.J. 2007 Hairpin vortex organization in wall turbulence. *Phys. Fluids* **19** (4), 041301.

ALKISHRIWI, N., MEINKE, M. & SCHRÖDER, W. 2008 Large-eddy simulation of streamwise-rotating turbulent channel flow. *Comput. Fluids* **37** (7), 786–792.

BOLOTNOV, I.A., LAHEY, R.T., DREW, D.A., JANSEN, K.E. & OBERAI, A.A. 2010 Spectral analysis of turbulence based on the DNS of a channel flow. *Comput. Fluids* **39** (4), 640–655.

BRETHOUWER, G. 2017 Statistics and structure of spanwise rotating turbulent channel flow at moderate Reynolds numbers. *J. Fluid Mech.* **828**, 424–458.

CASCIOLA, C.M., GUALTIERI, P., JACOB, B. & PIVA, R. 2005 Scaling properties in the production range of shear dominated flows. *Phys. Rev. Lett.* **95** (2), 024503.

CIMARELLI, A., DE ANGELIS, E. & CASCIOLA, C.M. 2013 Paths of energy in turbulent channel flows. *J. Fluid Mech.* **715**, 436–451.

CIMARELLI, A., DE ANGELIS, E., JIMENEZ, J. & CASCIOLA, C.M. 2016 Cascades and wall-normal fluxes in turbulent channel flows. *J. Fluid Mech.* **796**, 417–436.

CIMARELLI, A., DE ANGELIS, E., SCHLATTER, P., BRETHOUWER, G., TALAMELLI, A. & CASCIOLA, C.M. 2015 Sources and fluxes of scale energy in the overlap layer of wall turbulence. *J. Fluid Mech.* **771**, 407–423.

DAI, Y.-J., HUANG, W.-X. & XU, C.-X. 2016 Effects of Taylor–Görtler vortices on turbulent flows in a spanwise-rotating channel. *Phys. Fluids* **28** (11), 115104.

DAI, Y.J., HUANG, W.X. & XU, C.X. 2019 Coherent structures in streamwise rotating channel flow. *Phys. Fluids* **31** (2), 021204.

DANAILA, L., ANSELMET, F., ZHOU, T. & ANTONIA, R.A. 2001 Turbulent energy scale budget equations in a fully developed channel flow. *J. Fluid Mech.* **430**, 87–109.

DAVIDSON, P.A. 2013 *Turbulence in Rotating, Stratified and Electrically Conducting Fluids*. Cambridge University Press.

DENG, B.-Q. & XU, C.-X. 2012 Influence of active control on STG-based generation of streamwise vortices in near-wall turbulence. *J. Fluid Mech.* **710**, 234–259.

DUNN, D.C. & MORRISON, J.F. 2003 Anisotropy and energy flux in wall turbulence. *J. Fluid Mech.* **491**, 353–378.

GATTI, D., CHIARINI, A., CIMARELLI, A. & QUADRIO, M. 2020 Structure function tensor equations in inhomogeneous turbulence. *J. Fluid Mech.* **898**, A5.

HAMILTON, J.M., KIM, J. & WALEFFE, F. 1995 Regeneration mechanisms of near-wall turbulence structures. *J. Fluid Mech.* **287**, 317–348.

HILL, R.J. 2002 Exact second-order structure-function relationships. *J. Fluid Mech.* **468**, 317–326.

HU, R., LI, X. & YU, C. 2022 Effects of the Coriolis force in inhomogeneous rotating turbulence. *Phys. Fluids* **34** (3), 035108.

JIMÉNEZ, J. 2011 Cascades in wall-bounded turbulence. *Annu. Rev. Fluid Mech.* **44**, 27–45.

JIMÉNEZ, J. & PINELLI, A. 1999 The autonomous cycle of near-wall turbulence. *J. Fluid Mech.* **389**, 335–359.

JING, Z. & DUCOIN, A. 2020 Direct numerical simulation and stability analysis of the transitional boundary layer on a marine propeller blade. *Phys. Fluids* **32** (12), 124102.

JOHNSTON, J.P., HALLEENT, R.M. & LEZIUS, D.K. 1972 Effects of spanwise rotation on the structure of two-dimensional fully developed turbulent channel flow. *J. Fluid Mech.* **56** (03), 533–557.

KIM, J. & MOIN, P. 1986 The structure of the vorticity field in turbulent channel flow. Part 2. Study of ensemble-averaged fields. *J. Fluid Mech.* **162**, 339–363.

KOLMOGOROV, A.N. 1941 The local structure of turbulence in incompressible viscous fluid for very large Reynolds numbers. *C. R. Acad. Sci. USSR* **30**, 301–305.

KRISTOFFERSEN, R. & ANDERSSON, H.I. 1993 Direct simulations of low-Reynolds-number turbulent flow in a rotating channel. *J. Fluid Mech.* **256**, 163–197.

LUMLEY, J. 1964 Spectral energy budget in wall turbulence. *Phys. Fluids* **7** (2), 190–196.

MARATI, N., CASCIOLA, C.M. & PIVA, R. 2004 Energy cascade and spatial fluxes in wall turbulence. *J. Fluid Mech.* **521**, 191–215.

MARUSIC, I. & MONTY, J.P. 2019 Attached eddy model of wall turbulence. *Annu. Rev. Fluid Mech.* **51** (July), 49–74.

MASUDA, S., FUKUDA, S. & NAGATA, M. 2008 Instabilities of plane Poiseuille flow with a streamwise system rotation. *J. Fluid Mech.* **603**, 189–206.

MININNI, P.D., ALEXAKIS, A. & POUQUET, A. 2009 Scale interactions and scaling laws in rotating flows at moderate Rossby numbers and large Reynolds numbers. *Phys. Fluids* **21** (1), 015108.

MIZUNO, Y. 2016 Spectra of energy transport in turbulent channel flows for moderate Reynolds numbers. *J. Fluid Mech.* **805**, 171–187.

MOLLICONE, J.P., BATTISTA, F., GUALTIERI, P. & CASCIOLA, C.M. 2018 Turbulence dynamics in separated flows: the generalised Kolmogorov equation for inhomogeneous anisotropic conditions. *J. Fluid Mech.* **841**, 1012–1039.

OBERLACK, M. 2001 A unified approach for symmetries in plane parallel turbulent shear flows. *J. Fluid Mech.* **427**, 299–328.

OBERLACK, M., CABOT, W., PETTERSSON REIF, B.A. & WELLER, T. 2006 Group analysis, direct numerical simulation and modelling of a turbulent channel flow with streamwise rotation. *J. Fluid Mech.* **562**, 383–403.

OBERLACK, M., CABOT, W.H. & ROGERS, M.M. 1999 Turbulent channel flow with streamwise rotation: Lie group analysis, DNS and modeling. In *First Symposium on Turbulence and Shear Flow Phenomena*, pp. 85–90. Begel House.

POPE, S.B. 2000 *Turbulent Flows*. Cambridge University Press.

RECKTENWALD, I., ALKISHRIWI, N. & SCHRÖDER, W. 2009 PIV–LES analysis of channel flow rotating about the streamwise axis. *Eur. J. Mech. (*B*/Fluids)* **28** (5), 677–688.

RECKTENWALD, I., WELLER, T., SCHRÖDER, W. & OBERLACK, M. 2007 Comparison of direct numerical simulations and particle-image velocimetry data of turbulent channel flow rotating about the streamwise axis. *Phys. Fluids* **19** (8), 085114.

RUSSO, S. & LUCHINI, P. 2017 A fast algorithm for the estimation of statistical error in DNS (or experimental) time averages. *J. Comput. Phys.* **347**, 328–340.

SMITH, L.M. & WALEFFE, F. 1999 Transfer of energy to two-dimensional large scales in forced, rotating three-dimensional turbulence. *Phys. Fluids* **11** (6), 1608–1622.

WU, H. & KASAGI, N. 2004 Effects of arbitrary directional system rotation on turbulent channel flow. *Phys. Fluids* **16** (4), 979–990.

XIA, Z., SHI, Y. & CHEN, S. 2016 Direct numerical simulation of turbulent channel flow with spanwise rotation. *J. Fluid Mech.* **788**, 42–56.

YAN, Z., LI, X. & YU, C. 2022 Helicity budget in turbulent channel flows with streamwise rotation. *Phys. Fluids* **34** (6), 065105.

YANG, Z., DENG, B.Q., WANG, B.C. & SHEN, L. 2018 Letter: the effects of streamwise system rotation on pressure fluctuations in a turbulent channel flow. *Phys. Fluids* **30** (9), 1–7.

YANG, Z., DENG, B.-Q., WANG, B.-C. & SHEN, L. 2020*a* On the self-constraint mechanism of the cross-stream secondary flow in a streamwise-rotating channel. *Phys. Fluids* **32** (10), 105115.

YANG, Z., DENG, B.-Q., WANG, B.-C. & SHEN, L. 2020*b* Sustaining mechanism of Taylor–Görtler-like vortices in a streamwise-rotating channel flow. *Phys. Rev. Fluids* **5** (4), 044601.

YANG, Y.T., SU, W.D. & WU, J.Z. 2010 Helical-wave decomposition and applications to channel turbulence with streamwise rotation. *J. Fluid Mech.* **662**, 91–122.

YANG, Z. & WANG, B.-C. 2018 Capturing Taylor–Görtler vortices in a streamwise-rotating channel at very high rotation numbers. *J. Fluid Mech.* **838**, 658–689.

YEUNG, P.K. & ZHOU, Y. 1998 Numerical study of rotating turbulence with external forcing. *Phys. Fluids* **10** (11), 2895–2909.

YU, C., HU, R., YAN, Z. & LI, X. 2022 Helicity distributions and transfer in turbulent channel flows with streamwise rotation. *J. Fluid Mech.* **940**, A18.